NASA Contractor Report 3811

Interference Drag in a Simulated Wing-Fuselage Juncture

L. R. Kubendran, H. McMahon,
and J. Hubbartt
Georgia Institute of Technology
Atlanta, Georgia

Prepared for
Langley Research Center
under Grant NAG1-306

National Aeronautics
and Space Administration

**Scientific and Technical
Information Branch**

1984

Use of trade names or names of manufacturers in this report does not constitute an official endorsement of such products or manufacturers, either expressed or implied, by the National Aeronautics and Space Administration.

SUMMARY

The interference drag in a wing-fuselage juncture as simulated by a flat plate and a body of constant thickness having a 1.5:1 elliptical leading edge is evaluated experimentally.

The experimental measurements consist of mean velocity data taken with a hot wire at a streamwise location corresponding to 16 body widths downstream of the body leading edge. From these data, the interference drag is determined by calculating the total momentum deficit (momentum area) in the juncture and also in the two-dimensional turbulent boundary layers on the flat plate and body at locations sufficiently far from the juncture flow effect.

The interference drag caused by the juncture is small and negative, i.e., a slightly favorable interference effect. The interference drag as measured at this particular streamwise station is -3% of the total drag due to the flat plate and body boundary layers in isolation. If the body is considered to be a wing having a chord and span equal to 16 body widths, the interference drag due to the juncture is only -1% of the frictional drag of one surface of such a wing.

The effects of the secondary flow in the juncture are confined to a region extending approximately 2.6 body widths along the flat plate and 0.90 body widths along the body surface perpendicular to the flat plate.

INTRODUCTION

Flow in the juncture or corner formed by a wing and a fuselage has been of concern to aerodynamicists for many years because of interference effects and their impact on vehicle drag and stall. As early as the 1920's, the geometry between the wing and the fuselage was examined by making force measurements on filleted junctures (ref. 1). Recently, the wing-fuselage interference drag problem has received renewed attention because interference effects have increased in importance as a consequence of the achievement of large total drag reductions for the overall vehicle and also because increases in fuel costs have served as a motivation for re-examining all aspects of aircraft drag.

Wing-fuselage interference is of two primary types, potential flow interference and boundary layer interference. The latter type, for turbulent boundary layers, is of concern here. Drag due to this boundary layer interference occurs because the flow in the wing-fuselage juncture is markedly different from the conventional boundary layer flow on each surface when considered separately. This is due to the presence of a strong secondary flow in the juncture, i.e., there are significant velocity components normal to the main flow direction. Just as in the case of two flat plates with coincident leading edges, there is a secondary flow set up in a wing-fuselage juncture due to Reynolds stress gradients. However, this type of secondary flow is overshadowed by two larger effects. When an obstruction, such as a wing, projects from a surface, such as a fuselage, the oncoming turbulent boundary layer skews as it passes around the obstruction. This skewing stretches and rotates the vortex lines within the approaching boundary layer, producing a streamwise vorticity in the juncture. Secondly, the blockage associated with the presence of the obstruction causes the oncoming boundary layer to experience steep adverse pressure gradients in the vicinity of the body leading edge. As a result, the boundary layer generally separates and a strong vortex sheet rolls up and trails downstream in the juncture. Commonly, this trailing vortex is the dominant juncture flow feature. These two mechanisms for depositing streamwise vorticity into the corner are shown schematically in figure 1.

Juncture interference drag is here taken to be the difference in drag of the two wing-fuselage components taken first in isolation and summed and then taken in combination. It is made up of three parts. The first is the change in the surface shear stress caused by the merging of the two boundary layers and by the distortion of the velocity profiles in the juncture due to the secondary flow present in the juncture. The second part is the induced drag attributable to a loss of energy to the secondary flow in the juncture, the major contributor to the induced drag being the vortex formed by the boundary layer separation and roll-up. The third element of the interference drag is the change in pressure drag brought about by the modified growth of the viscous layer in the juncture.

In recent years, the interference drag problem has been considered by several investigators. Hawthorne (ref. 2) used an inviscid small perturbation analysis. The case of a wing or strut projecting from a wall along which a boundary layer is developing was treated by assuming a non-uniform upstream profile which varied in the spanwise direction in the manner of a boundary layer profile. The drag deduced from the kinetic energy in the secondary flow was compared with experimental drag measurements on a

strut (ref. 3). It was concluded from the considerable discrepancy between the measured drag and the calculated (and also measured) energy in the secondary flow that the disturbance of the boundary layer on the strut must be considered if one is to fully account for the interference drag.

Gersten (refs. 4, 5) studied the interference drag in a right-angle corner formed by two flat plates with coincident leading edges. He concluded that the frictional resistance in the turbulent case is larger for the corner flow as compared with two flat plates without interference, but that the increase is less than 1% of the drag without interference. In contrast, Schlichting (ref. 6) quotes Gersten's results as indicating that the supplementary frictional drag is negative, meaning that the drag of two flat plates joined at right angles is smaller than the drag of a flat plate of equal total area.

Hoerner (ref. 7) presents experimental data for the interference drag at the junction of wings or struts with a plane wall. He states that the results suggest that the interference drag will be negative (i.e., favorable interference) at thickness ratios below about 8%.

Barber (ref. 8) points out the lack of interference drag data for flow around struts in gas turbines. He made total pressure surveys 0.4 chordlengths downstream of the trailing edge of a strut mounted on a flat plate and the drag of the intersection was obtained from a momentum balance. It was concluded that the intersection loss was small if the boundary layer on the plate at the strut leading edge was thick (12% of the strut chord). The loss was larger, especially with increasing angle of incidence of the strut, if the leading edge of the strut and plate were essentially coincident. These drag measurements were made downstream of the strut trailing edge and included the influence of the viscous wake of the strut.

The preceding review illustrates that the magnitude (and even the sign) of the boundary layer interference drag in a juncture is an open question. The purpose of the work reported here was to evaluate this drag for a simple juncture geometry.

The juncture flow investigated in this work was generated by a constant thickness body ("wing"), having an elliptical leading edge, which was mounted perpendicular to a large flat plate ("fuselage") along which a turbulent boundary layer was developing (fig. 2). The interference drag was determined from the momentum deficits calculated at a fixed streamwise station, first for the two-dimensional boundary layers on the body and on the plate and then for the three-dimensional viscous flow in the juncture. These calculations were carried out by using values of the local mean velocity component in the streamwise (x) direction as determined from hot-wire measurements. The hot-wire

measurements also supplied data from which the induced drag, due to the secondary flow in the juncture, could be evaluated.

The equipment and instrumentation used in these experiments, as well as most of the data analysis and data acquisition procedures, are the same as those reported earlier in references 9 and 10. A summary of each will be given here for completeness. A detailed discussion of the model and actuator is found in reference 11.

SYMBOLS

A-F	Constants used in data reduction, defined in equations 9-14
c_f	Skin friction coefficient
D_{int}	Interference drag expressed as fraction of drag due to flat plate plus body each in isolation
$D_{int(w)}$	Interference drag expressed as fraction of drag of reference wing
e_ℓ	AC component of E_ℓ, volts
E	Nonlinear output voltage of constant-temperature anemometer, volts
E_ℓ	Linearized output voltage of hot-wire anemometer, volts
E_o	Output voltage of hot-wire anemometer at zero velocity, volts
h	Binormal velocity coefficient (eq. 2)
I	Induced drag due to secondary flow (eq. 41), N
k	tangential velocity coefficient (eq. 2)
K_y	Cumulative momentum deficit with integration in y direction (eq. 29), N
K_z	Cumulative momentum deficit with integration in z direction (eq. 27), N
p	Static pressure, N/m^2
Δp	$p - p_a$, N/m^2
q	Dynamic pressure, N/m^2
s, y, n	Hot-wire coordinate system (figs. 7 and 8)
S	Constant of proportionality (eq. 4), volts/m/s
T	Total momentum deficit or momentum area (eq. 30), N
ΔT	Difference between total momentum deficit in juncture and total momentum deficits in plate and body boundary layers (eq. 36), N
u	Varying instantaneous velocity, m/s
U	Local mean or time-averaged velocity, m/s

U_{BN}	Binormal velocity component, normal both to U_N and U_T (eq. 2), m/s
U_{eff}	Effective cooling velocity (eq. 2), m/s
U_N	Velocity component normal to hot wire in plane of wire-support needles (eq. 2), m/s
U_T	Velocity component tangent to the hot wire (eq. 2), m/s
U_τ	Shear velocity (figs. 14, 15), m/s
x, y, z	Laboratory coordinate system (figs. 7 and 8)
α , β , λ , ψ	Angles expressing hot-wire orientation (fig. 8), degrees
δ	Error term (App. A)
ϵ	Collection of terms in expression for U_{eff} (eq. 8)
θ	Momentum thickness (eq. 24), mm
ν	Kinematic viscosity, m^2/s
ρ	Mass density, kg/m^3

Subscripts:

a	Ambient conditions
B	Indicates that quantity is evaluated for constant-thickness body in isolation
e	Indicates that quantity is evaluated at the edge of the viscous layer
J	Indicates that quantity is evaluated for juncture flow
ℓ	Linearized output
n	Component in n direction
P	Indicates that quantity is evaluated for flat plate in isolation
s	Component in s direction
x	Component in x direction
y	Component in y direction; also value of variable at general or specific value of y
z	Component in z direction; also value of variable at general or specific value of z
α , ψ	Indicates that quantity is evaluated with wire angles α and ψ (fig. 8)

Superscripts:

*	Indicates value derived using approximate value of U_s from equation A-2 (App. A)
—	Time average of quantity

EQUIPMENT

Wind Tunnel

The experiments were carried out in the Georgia Tech Low Speed Wind Tunnel, which is an open return type with a velocity continuously variable to a maximum of 22.9 m/s (75 ft./s). The test section is 1.07 x 1.09 x 6.10 m (42 x 43 x 240 in.) and the freestream turbulent intensity near the exit of the test section was measured to be 0.5%.

Body and Flat Plate

The body and flat plate were mounted in the free jet at the exit of the open return wind tunnel (fig. 2) in order to simplify the moving of the measurement probes over a considerable distance in the transverse direction.

The body, which was mounted perpendicular to the flat plate and aligned with the wind tunnel axis, consisted of a leading edge which is a 1.5:1 ellipse attached to an afterbody of constant thickness 56.9 mm (2.28 in.) and having a length of 1.22 m (48 in.). The leading edge of the body had a strip of distributed glass-bead roughness, (average bead diameter 0.25 mm (0.01 in.)), which was 6.35 mm (0.25 in.) wide beginning 25.4 mm (1.0 in.) downstream of the nose. The nose of the body was located 229 mm (9.0 in.) downstream of the wind tunnel exit plane.

The flat plate was mounted above the floor of the wind tunnel and an extension of the plate, which served as a boundary layer development section, protruded 572 mm (22.5 in.) upstream into the wind tunnel. The flat plate was fitted with a trip wire 0.97 mm (0.038 in.) in diameter located 102 mm (4.0 in.) downstream of the leading edge. The plate (fig. 2) was made with interchangeable segments so that the particular segment containing the probe and actuator (fig. 3) could be located at several streamwise stations. Since measurements reported here were made at a fixed streamwise station, the interchangeability feature was not used. The segments were adjusted so that the mismatch at any joint between segments was at most $\pm$0.13 mm (0.005 in.) compared to a nominal boundary thickness at the measurement station of 38 mm (1.5 in.).

Static Pressure Probes

As a preliminary step before the evaluation of the momentum deficits it was necessary to know whether the static pressure in the juncture was the same as that at the edge of the undisturbed two-dimensional boundary layer growing on the flat plate when the body was removed. This was necessary because a comparison of the momentum deficits for these two cases was to be made later as part of the determination of the interference drag. Also, it was essential to know whether there were any appreciable lateral (z) static pressure gradients in the freestream juncture flow since these would affect the velocity profiles and hence the momentum deficit.

Three static pressure probes were constructed. All three had the same geometry (fig. 4) but the static pressure holes were located differently. As will be explained later, the static pressure probe in the juncture could be aligned with the local mean flow direction as regards yaw but not pitch. Therefore, one of the probes (detail A, fig. 4) had the holes located so as to minimize upflow effects and the second (detail B, fig. 4) downflow effects. The third probe (detail C, fig. 4) was planned as an evaluation probe to assess the effect of flow misalignment on a measured static pressure by yawing the probe in the freestream to simulate flow pitch effects.

Hot Wires

Two different hot-wire geometries as well as two different probe configurations were used in this investigation, for a total of four hot-wire sensors. The two configurations of probes were needed to make measurements at different heights above the plate surface. The two different hot-wire geometries were needed to determine the various velocity components. One probe configuration was the same as that used earlier by the authors in measurements of mean flow and turbulence quantities upstream of and within the juncture (refs. 9 and 10). The two wire geometries for this configuration are illustrated in figure 5. Since the hot-wire sensors for these probes were supported on needles which protruded through the surface of the flat plate, the vertical travel of the sensors was limited by the length of the needles. However, the current tests required measurements to be made at a greater distance from the plate surface than in the previous work. Thus the two different hot-wire geometries used previously were reproduced but with the needles supported vertically by a tube of diameter 3.18 mm (0.125 in.) which protruded through the surface of the flat plate.

The hot-wire geometry with the wire held parallel to the plate surface (i.e., support needles of equal length) is shown in figure 5(a) and is called the "horizontal wire." For the probe with the needles protruding through the plate, the needles were 3.18 mm (0.125 in.) apart and supported a platinum-coated tungsten wire 0.0051 mm (0.0002 in.) in diameter with an etched center portion 1.27 mm (0.050 in.) long. The probe needles could be extended to a maximum height above the plate surface, y, of approximately 35.6 mm (1.40 in.) and rotated a full 360° about the probe axis. For the other horizontal-wire probe configuration with the needles supported by a tube, the needle diameter and hot wire were unchanged, and the fixed needle length above the tube was 13 mm (0.5 in.). This probe was used for detailed measurements between y = 25.4 mm (1.0 in.) and y = 94 mm (3.7 in.), the smaller value allowing for data overlap with the horizontal wire supported through the plate surface.

Since the evaluation of the velocity components required the use of a hot wire oriented at an angle to the surface of the flat plate, a second hot-wire geometry was obtained with needles of unequal length (fig. 5(b)) called the "slant wire." In order that the wire not be in the wake of the longer needle at certain angular orientations as the probes rotated about their axis, the longer needle was offset by a distance of 5.1 mm (0.20 in.) for both probes. The wire was the same type and diameter as the horizontal wire and was 4.5 mm (0.177 in.) long. Because of the needle geometry, the sensor portion of the slant wire supported through the plate was limited to an excursion in y, the distance above the plate surface, of 2.3 mm < y < 28 mm (0.090 in. < y < 1.10 in.). The slant wire mounted on the tube was used over the same range in y as that for the horizontal wire. The slant wire orientation angle, α, was approximately 45° for both probes and was evaluated to $\pm 0.05^\circ$ by using an optical comparator. Both of the slant wire probes could be rotated 360° about the probe axis.

Since both types of wire geometries (horizontal and slant wire) had to be used sequentially in order to determine all of the required mean flow data, and since the wires supported on the tubes in effect provided an extension of travel of the hot wires supported by the needles through the plate, it was important that the sensor portion of each wire be located at nearly the same point when the various probes were interchanged. This was accomplished to an accuracy of ±0.025 mm (0.001 in.) using special optics and techniques (ref. 9) developed for this purpose. Including this uncertainty, it is estimated that the y location of the probes was accurate to within ±0.05 mm (0.002 in.) while the z location was accurate to within ±0.10 mm (0.004 in.).

All probes were calibrated by locating the sensor portion of the wire at the outer edge of the boundary layer or in the freestream at an orientation such that the wire was normal to the local velocity vector. The output voltage was measured in this flow where the local velocity was determined from simultaneous measurements with a pitot-static probe.

Actuator Linear Motion

The segment of the flat plate which contained the static pressure and hot-wire probes consisted of a slide and slide bed (fig. 3). The probes were held in an actuator which hung below the slide and moved with the slide.

The streamwise (x) location of the survey station was fixed. Linear movements of the probes in directions perpendicular to the plate (y) and normal to the body surface (z) were accomplished by using lead screws driven by stepper motors.

Actuator Angular Motion

In addition to linear motion, the probes had to be rotated about their own axes in order to generate the necessary data. The local flow yaw angle, β, was found with the horizontal wire and formed the basis for the coordinate system used in taking the remainder of the data. The determination of this angle involved a measurement of both the reference main flow direction (i.e., the x axis) and the local flow direction. The uncertainty in the magnitude of the local skew angle, β, is estimated to be $\pm 1.0^{\circ}$. Using the special optics mentioned above, the angular position of the slant wires could be set to the flow direction to within less than 0.5°.

INSTRUMENTATION AND PROCEDURES

Freestream Velocity

The velocity of the wind tunnel flow was measured with a pitot-static probe. The dynamic pressure was read with a Barocel electronic manometer and digital voltmeter, and the wind tunnel velocity was held constant to within $\pm 0.5\%$ and was in error by less than $\pm 0.5\%$.

Hot-wire velocity calibration during the juncture flow measurements was accomplished by using a pitot-static probe and hot-wire sensor located near each other and at $z = 152$ mm (6.0 in.) where the flow in the juncture is effectively two-dimensional.

Static Pressures

Measurements using the static pressure probe were made by connecting the pressure tubing to one side of a differential pressure Barocel transducer. The other side of the transducer was open to atmospheric pressure through a long piece of tubing in order to damp out small pressure fluctuations in the room. The Barocel signal conditioner output was fed to an HP 2401C integrating digital voltmeter, where the signal was integrated over one second five consecutive times and then arithmetically averaged.

Hot-Wire Anemometer

The hot-wire probes were connected to a TSI Model 1050 anemometer, with the output of the anemometer going to a TSI Model 1052 polynominal linearizer.

Local Mean Velocity

The linearized output of the anemometer was read with an HP 2401C integrating digital voltmeter. This voltmeter was set for maximum integrating time (1.0s). Mean D.C. voltages were taken by arithmetically averaging 30 individual voltmeter samples (i.e., a total of 30 seconds of integration) for U_y and for U_s. A discussion of the choice of averaging times is found in Appendix A of reference 9.

Data Handling

Movement of the actuator stepper motors as well as all data acquisition were controlled in real time by an on-site computer. The voltage output from the digital voltmeter was monitored on an HP 2645A terminal and either stored temporarily in a cartridge tape unit or transmitted through a direct line to an HP 21MX-E Series computer for disc storage and later data reduction.

Operating Conditions

All of the tests were run at a nominal freestream velocity of 15.24 m/s (50 ft./s) giving a Reynolds number of 994,000/m (300,000/ft.). The turbulent boundary layer thickness on the flat plate at the streamwise location corresponding to the leading edge of the body was approximately 22.9 mm (0.9 in.), giving a ratio of boundary layer thickness to body thickness of 40%.

Measurements were made in the juncture at a fixed location 902 mm (35.5 in.) downstream of the leading edge of the body and also were made at this same streamwise station in the flat plate boundary layer with the body removed.

Coordinate Systems

Two Cartesian coordinate systems were employed in this work (fig. 6). The first coordinate system was the working coordinate system s-y-n used in the taking of data in the juncture. The local yaw angle, β, was found for each value of y and z using the horizontal hot wire. This value of β defined a local s-y-n coordinate system which rotated about the vertical y axis as the value of y changed (fig. 7).

The second coordinate system was the x-y-z coordinate system used for data analysis. These are wind tunnel or laboratory coordinates, with x in the freestream direction, y perpendicular to the surface of the flat plate, and z normal to the body surface (figs. 2 and 6). The laboratory coordinates are defined such that $x = 0$ at the leading edge of the body, $y = 0$ at the plate surface, and $z = 0$ on the body surface.

General Method

It will be recalled from the Introduction that the approach used here for evaluating the interference drag was to determine it from momentum deficits calculated from measured mean velocity profiles. The reference condition (plate and body in isolation) was obtained by measuring profiles in the two-dimensional boundary layer on the flat plate with the body removed and also in the boundary layer on the body surface at a sufficiently large distance above the plate so that two-dimensional conditions prevailed. The momentum deficit to be compared with this reference was that calculated from velocity profiles measured in the juncture. The juncture measurements were carried out to values of y and z which were large enough to ensure

that the juncture viscous layer had approached the two-dimensional condition on both surfaces. That is, in evaluating the total momentum deficit due to the juncture there must be assurance that all of the change in momentum deficit has been accounted for and that at larger values of y and z the flow will be two-dimensional so that the momentum deficit will cancel when a difference is taken with the sum of the two-dimensional deficits on the two surfaces in isolation.

In the two-dimensional boundary layer for the isolated flat plate, measurements of U_s and U_y were made at 7 values of z between z = 0 and z = 152 mm (6.0 in.) and at 34 values of y through the boundary layer between y = 0 and y = 94 mm (3.7 in.), all at a streamwise location corresponding to x = 902 mm (35.5 in.). The spacing in y and z was larger for the static pressure measurements.

In the juncture of the two surfaces, the horizontal wires were used first to establish the local flow direction, β, and the velocity component U_s. Next, the slant wire probes were used to measure U_y for calculation of secondary flow induced drag. As will be explained in the next section, two measurements with the slant wire at $\psi = 0^\circ$ and $\psi = 180^\circ$ were sufficient to establish U_y. Finally, the static pressure probe was installed and was aligned at the local yaw angle, β, at each vertical measurement station prior to the measurement of static pressure. This alignment minimized any measurement error due to yaw. The configuration of the static pressure probe was such that the pressure measurements were made 50.8 mm (2.0 in.) upstream of the velocity measurement station. However, static pressure taps in the slide bed showed that the streamwise pressure gradient over this interval was negligible.

In the juncture, measurements of U_s and U_y were made at 19 transverse (z) stations and at 34 vertical (y) locations at each z. These stations are detailed in Table 1. Spacing in y and z was slightly larger for the static pressure measurements.

With the two mean velocity components and the local yaw angle, β, known at each location, the streamwise velocity component, U_x, as well as the components U_y and U_z are determined.

After suitable adjustment for static pressure level (see Results and Discussion) the U_x velocity profiles on the flat plate and in the juncture were integrated to yield the momentum thickness, θ, for various y or z measurement stations. As will be seen later, the viscous layer on the surface of the vertical body becomes two-dimensional at rather small values of y, namely for $y \geq 50.8$ mm ($y \geq 2.0$ in.).

The total momentum deficit in the juncture was evaluated by integrating the calculated values of the momentum deficit for the juncture over a rectangular area

normal to the freestream direction (i.e., a momentum area was evaluated). This rectangular area was made large enough so that outside it the boundary layers on the two mating surfaces were two-dimensional in character. The interference then was interpreted as the total momentum deficit over the rectangular area in the juncture minus the sum of the two-dimensional reference momentum areas. In the case of the flat plate, the momentum area was the integral of the momentum deficit over a transverse distance, z, equal to the width of the rectangle. For the body, the reference momentum area was formed as the product of the two-dimensional momentum thickness, θ, at y = 76 mm (3.0 in.) and a length corresponding to the height of the rectangle.

The energy loss to the secondary flow in the juncture (induced drag) was evaluated by calculating the quantity $\frac{1}{2} \rho \left(U_y^2 + U_z^2 \right)$ at each measurement station and then integrating over the area of the same rectangle.

Data Quality Control

The hot-wire calibrations and the polynomial coefficients for the linearizer were updated periodically as required. Close attention was paid to drift in the electronic instruments, and compensation was made for variations in the temperature of the wind tunnel air as described in Appendix B of reference 9. The output of the hot-wire probes was monitored continuously on an oscilloscope to detect any signs of wire or probe vibration. Particular care was taken when the hot wires mounted on the tubes were used at large values of y. In these cases, the root-mean-square output of the wires was recorded and the data were examined for any unusual behavior.

The repeatability of the measured mean velocity profiles in the juncture with those taken previously (ref. 9) was very good. However, new data were taken here in order to have a consistent data set. Also, the spacing of the data in y and z is much closer than in reference 9 because of the required integrations.

DATA ACQUISITION AND ANALYSIS

The hot wire is shown schematically in figure 8 with an arbitrary orientation in both the laboratory (x-y-z) and hot-wire (s-y-n) Cartesian coordinate systems. In both coordinate systems y is measured normal to the flat plate whereas x, z, s, and n are in the plane of the plate. The hot-wire coordinates were used for data acquisition and the results then were transformed into laboratory coordinates.

The orientation of the hot wire in the wire coordinate system is specified by the two angles α and ψ shown in figure 8. The angle α is the angle between the axis of rotation and a normal to the wire defined to be in the plane containing the hot wire and the axis of rotation. The angle ψ is the angle between the s axis and the projection of the hot wire on the s-n plane (i.e., on the plane of the flat plate).

The nonlinearized voltage output of the constant-temperature anemometer is related to α, ψ, and the three instantaneous velocity components. That is,

$$E = E(U_s + u_s, U_y + u_y, u_n, \alpha, \psi)$$

In order to linearize this relationship between the voltage output and the instantaneous flow velocity, it is necessary to introduce an effective cooling velocity, U_{eff}, such that

$$E = E(U_{eff}) \tag{1}$$

where

$$U_{eff} = f(U_s + u_s, U_y + u_y, u_n, \alpha, \psi)$$

This functional relationship for U_{eff} must be determined by calibration. For the present investigation, the relationship suggested by Jorgensen (ref. 12) was used. This expression is

$$U_{eff} = (U_N^2 + k^2 U_T^2 + h^2 U_{BN}^2)^{1/2} \tag{2}$$

where U_N is the velocity component normal to the wire in the plane of the wire-support needles, U_T is the velocity component tangent to the wire, and U_{BN} is the binormal velocity component which is normal to both U_N and U_T. The coefficients k and h are determined by calibration. In terms of the angles and the coordinate system of figure 8 equation (2) becomes

$$U_{eff} = \left\{ \left\{ \left[(U_s + u_s)\cos\psi + u_n \sin\psi \right] \sin\alpha - (U_y + u_y)\cos\alpha \right\}^2 + k^2 \left\{ \left[(U_s + u_s)\cos\psi + u_n \sin\psi \right] \cos\alpha + (U_y + u_y)\sin\alpha \right\}^2 + h^2 \left\{ -(U_s + u_s)\sin\psi + u_n \cos\psi \right\}^2 \right\}^{1/2} \quad (3)$$

The relation between U_{eff} and E, as expressed by equation (1), was determined by experiment for the four wires used in this study. These data then were used along with the linearizer circuit of the constant-temperature anemometer to generate, for each wire, a linearized output voltage E_ℓ which is directly proportional to U_{eff}. Thus

$$E_\ell = SU_{eff} \quad (4)$$

where S is a constant of proportionality depending upon the particular hot wire. E_ℓ is decomposed into a mean or DC component, $\bar{E}_\ell$, and a fluctuating or AC component, e_ℓ, where $\bar{e}_\ell = 0$, so that equation (4) becomes

$$\bar{E}_\ell + e_\ell = SU_{eff} \quad (5)$$

In this equation, $\bar{E}_\ell$ and the root-mean-square of e_ℓ (i.e., $\sqrt{\overline{e_\ell^2}}$) are measurable quantities which can be related to the velocities. Taking the mean of equation (5) gives

$$\frac{\bar{E}_\ell}{S} = \bar{U}_{eff} \quad (6)$$

Equations (3) and (6) yield an equation relating $\bar{E}_\ell$ to mean values of the various velocity components for fixed values of α and ψ.

To relate $\bar{E}_\ell$ to the unknowns using equation (6), it is necessary to evaluate $\bar{U}_{eff}$ from equation (3). The evaluation of $\bar{U}_{eff}$ requires that equation (3) be expanded in a truncated Taylor's series. For the hot-wire axes of figure 8, U_s is the only zeroth order velocity component while U_y, u_s, u_y, and u_n are first order terms. Therefore, for this analysis equation (3) was expanded in a series and then averaged over time to obtain $\bar{U}_{eff}$. This expression for $\bar{U}_{eff}$ was truncated by neglecting third and higher order terms. After squaring and collecting terms under the square root radical, equation (3) may be rewritten in the form

$$U_{eff} = U_s \sqrt{A}\,(1 + \varepsilon)^{1/2} \tag{7}$$

where ε involves first and second order terms and is given by

$$\varepsilon = 2\frac{u_s}{U_s} + \left(\frac{u_s}{U_s}\right)^2 + B\left[\left(\frac{U_y}{U_s}\right)^2 + 2\frac{U_y u_y}{U_s U_s} + \left(\frac{u_y}{U_s}\right)^2\right]$$

$$+ C\left(\frac{u_n}{U_s}\right)^2 + D\left(\frac{U_y}{U_s} + \frac{u_y}{U_s} + \frac{u_s}{U_s}\frac{U_y}{U_s} + \frac{u_s}{U_s}\frac{u_y}{U_s}\right)$$

$$+ E\left(\frac{U_y u_n}{U_s U_s} + \frac{u_y u_n}{U_s U_s}\right) + F\left(\frac{u_n}{U_s} + \frac{u_s u_y}{U_s U_s}\right) \tag{8}$$

where

$$A = \cos^2\psi \sin^2\alpha + k^2 \cos^2\psi \cos^2\alpha + h^2 \sin^2\psi \tag{9}$$

$$B = (\cos^2\alpha + k^2 \sin^2\alpha)/A \tag{10}$$

$$C = (\sin^2\psi \sin^2\alpha + k^2 \sin^2\psi \cos^2\alpha + h^2 \cos^2\psi)/A \tag{11}$$

$$D = 2(\cos\psi \sin\alpha \cos\alpha)(k^2 - 1)/A \tag{12}$$

$$E = 2(\sin\psi \sin\alpha \cos\alpha)(k^2 - 1)/A \tag{13}$$

$$F = 2 \cos\psi \sin\psi (\sin^2\alpha + k^2 \cos^2\alpha - 2h^2)/A \tag{14}$$

Expanding equation (8) in a Taylor's series and dropping terms of ε^3 and higher order, and introducing the results into equation (6) gives

$$\frac{\bar{E}_\ell}{S} = U_s \sqrt{A}\left(1 + \frac{1}{2}\bar{\varepsilon} - \frac{1}{8}\overline{\varepsilon^2}\right) \tag{15}$$

Finally, using equation (8) to evaluate $\bar{\varepsilon}$ and $\overline{\varepsilon^2}$ and dropping third and higher order terms, equation (15) becomes, after rearranging,

$$\frac{\bar{E}_\ell}{S} = U_s \sqrt{A}\left[1 + \left(\frac{B}{2} - \frac{D^2}{8}\right)\left(\frac{U_y^2}{U_s^2} + \frac{\overline{u_y^2}}{U_s^2}\right) + \frac{D}{2}\frac{U_y}{U_s}\right.$$

$$\left. + \left(\frac{C}{2} - \frac{F^2}{8}\right)\frac{\overline{u_n^2}}{U_s^2} + \left(\frac{E}{2} - \frac{DF}{4}\right)\frac{\overline{u_y u_n}}{U_s^2}\right] \tag{16}$$

Equation (16) is the general form of the hot-wire response equation used for evaluating the unknown velocity terms. $\bar{E}_\ell$ is the measured quantity and S is the known calibration constant discussed later. This response equation is specialized for each of the two wire geometries at various values of ψ to evaluate the unknown velocity terms. The procedure and specific equations used to evaluate each velocity term are as follows:

(1) Evaluation of U_y. Applying equation (16) to the slant wire both with $\psi = 0$ and 180° yields

$$\frac{(\bar{E}_\ell)_{47.3,180}}{S} - \frac{(\bar{E}_\ell)_{47.3,0}}{S} = 2\,\frac{(1-k^2)\sin\alpha\,\cos\alpha}{(\sin^2\alpha + k^2\cos^2\alpha)^{1/2}}\,U_y \qquad (17)$$

where $\alpha = 47.3^\circ$. Equation (17) was used to evaluate U_y.

(2) Evaluation of U_s. Applying equation (16) to the horizontal wire with $\psi = 90^\circ$ yields

$$\frac{(E_\ell)_{0,90}}{S} = \frac{h}{U_s}\left[U_s^2 + \frac{1}{2h}\left(U_y^2 + \overline{u_y^2}\right) + \frac{k^2}{2h^2}\,\overline{u_n^2}\right] \qquad (18)$$

The third term on the right-hand side is a fourth order quantity and, therefore, was neglected. Thus, equation (18) can be rewritten as

$$\frac{(E_\ell)_{0,90}}{S} = hU_s\left[1 + \frac{1}{2h}\left(\frac{U_y^2}{U_s^2} + \frac{\overline{u_y^2}}{U_s^2}\right)\right] \qquad (19)$$

In the present data reduction procedure, the second term in the square bracket was neglected compared to the lead term unity. The mean velocity component U_y was evaluated at most data stations (Table 1) using the slant wire, and some extrapolation scheme could have been set up to estimate U_y at those stations very close to the plate surface or body surface where the slant wire geometry prohibited measurements. Thus, the U_y term in equation (19) could have been included in the data reduction scheme but it was neglected because the error introduced is negligible.

The term $\overline{u_y^2}/U_s^2$ in equation (19) also was neglected. While the turbulence quantity $\overline{u_y^2}$ presented no serious measurement problem, and in fact had been evaluated

in prior experiments (refs. 9, 10), the data necessary to evaluate $\overline{u_y^2}$ involve the measurement of RMS voltages using both the horizontal and slant wires, which is very time consuming. The data of reference 9 could not be used since the data stations in that earlier work were not as closely spaced as needed here. Hence, the decision was made that no turbulence quantities would be evaluated during the present measurements.

The magnitude of the neglected terms U_y and $\overline{u_y^2}$ may be estimated by examination of the data in figure 21 of reference 9. These data are nondimensionalized by V_∞ rather than by U_s, but U_s and U_x are essentially the same since the yaw angle, β, in the juncture is very small (less than 5 degrees) and plots of U_x/V_∞ are also given in figure 21. Figure 21 shows the variation of U_y and $\overline{u_y^2}$ in the juncture. However, the more important question is how much the quantities U_y/U_s and $\overline{u_y^2}/U_s^2$ differ from their two-dimensional boundary layer values, since the drag is to be interpreted as the difference between the total momentum deficit in the juncture and that for the sum of the two surface boundary layers in isolation. Taking the measured values at $z = 152.4$ mm (6.0 in.) as being typical for a two-dimensional boundary layer (fig. 21-a, ref. 9), the maximum change in these two quantities due to the presence of the juncture was estimated. The maximum possible error in the interference drag brought about by the simplification of equation (19) was evaluated (Appendix A) and found to be within the experimental error in the measurements. Accordingly, U_s was determined directly from the relation

$$\frac{(E_\ell)_{0,90}}{S} = hU_s \tag{20}$$

The use of equation (20) means that U_s can be found with satisfactory accuracy without using the measured values of U_y. Since U_s is the mean velocity component in a plane parallel to the surface of the flat plate and the yaw angle β is known, it follows that the streamwise mean velocity component needed for the momentum deficit calculations is simply

$$U_x = U_s \cos\beta \tag{21}$$

Likewise, since

$$U_z = U_s \sin\beta \tag{22}$$

and U_y has been measured, the energy loss to the secondary flow in the juncture may be expressed as an induced drag given by

$$I = q_e \iint \frac{U_y^2 + U_z^2}{U_e^2} \, dydz \tag{23}$$

RESULTS AND DISCUSSION

Static Pressure

Probe Evaluation. The static pressure probe designed for evaluation tests (detail C, fig. 4) was positioned in the freestream and rotated in yaw in order to simulate the effect of flow pitch angle on the measurement probes. It was found that within a simulated pitch angle of $\pm 4^o$ the change in $\Delta p/q_e$ was less than $\pm$ 0.5%. Since the maximum pitch angle to be expected in the juncture was about two degrees from the data of reference 9, it was concluded that the planned use of probes A and B (fig 4) on the upflow and downflow sides of the vortex core in the juncture so as to eliminate pitch errors was not necessary. The static probe when used in the juncture was always yawed to the measured local yaw angle β before a measurement was taken, so combined pitch and yaw effects were not present. Accordingly, probe A was used for all of the static pressure measurements reported here.

Static Pressure Data. The variation in static pressure through the two-dimensional boundary layer on the flat plate with the body removed is shown in figure 9. The static pressure measurements were taken at representative values of z between z = 0 and z = 152 mm (6.0 in.). A static pressure gradient through the boundary layer is observed which is larger than that attributable to turbulence ($\overline{u_y^2}$) as measured in this boundary layer during earlier studies (refs. 9, 10). Note that the values of $\Delta p/q_e$ in figure 9 are extremely small. For example, in a discussion of pressure instrumentation and particularly the effect of hole size on surface static pressures measurements, the authors of reference 13 typify a difference in $\Delta p/q_e$ of 0.004 as being "negligible." A band of $\pm$ .004 contains almost all of the data in figure 9.

Figure 10 shows a corresponding static pressure survey taken in the juncture in the vertical direction at four representative values of z. Again, the measured pressure gradient in the y direction is larger than that which could be attributed to $\overline{u_y^2}$ (ref. 9)

and, in fact, has almost the same slope as that measured in the flat plate boundary layer. The transverse (z) pressure gradient is small except very near the core of the secondary flow.

Comparing figures 9 and 10, it is noted that the level of $\Delta p/q_e$ at large y is almost zero for the flat plate and about -0.022 for the juncture. Recall that Δp was measured with a differential pressure transducer with one side open to the atmosphere in the wind tunnel room. These results thus indicate that the static pressure in the free jet above the flat plate was essentially ambient pressure. However, when the body was mounted on the plate the flow accelerated around the body and the static pressure in the juncture was less than ambient pressure.

Since momentum deficits were to be calculated for the flat plate boundary layer and also for the juncture flow, it was desirable that these deficits be calculated at the same static pressure level. Accordingly, all of the mean velocity components U_x as measured in the juncture were corrected for static pressure difference by a method due to Jones (ref. 14) and commonly used for correcting velocity measurements during the determination of profile drag from wake surveys. Using this method, all of the mean velocity values for U_x taken in the juncture were decreased by an amount which corresponded to increasing the freestream value of $\Delta p/q_e$ in the juncture from -0.022 to the flat plate freestream value of +0.003. No attempt was made to adjust individual velocity profiles in the juncture for static pressure variations in y or z since it was reasoned that the variations shown in figure 10 were caused by the juncture flow itself and should be charged against it in the later calculation of momentum deficit.

Mean Velocity Data

Four mean velocity profiles, U_x/U_e, are shown in figure 11 plotted against distance, y, above the plate surface for four selected values of z, the distance from the body surface. The profile at z = 152 mm (6.0 in.) is indicative of two-dimensional flow. Profiles at z = 51 mm (2.0 in.) and z = 25 mm (1.0 in.) are outboard and inboard, respectively, of the core of the secondary flow in the juncture. The profiles are distorted near the plate, as has been observed previously (ref. 9), and are constant when the edge of the viscous layer is reached. The profile at z = 2.5 mm (0.10 in.) is in the juncture flow near the plate surface and then is within the boundary layer on the body for larger values of y. The velocity U_x at this z-station is essentially constant for large values of y where the body boundary layer flow is two-dimensional.

The two-dimensional behavior of the body boundary layer for $y \geq 51$ mm ($y \geq 2.0$ in.) is emphasized in figure 12. This figure shows constant velocity contours in U_x looking downstream in the juncture. As noted previously (ref. 9), the effect of the secondary flow on the juncture mean flow inboard of the core of the secondary flow is to carry high momentum fluid from the edge of the viscous region downward toward the plate. Outboard of the core, low momentum fluid from near the plate surface is transported upward. These two effects lead to the distortion in the lines of constant velocity observed in figure 12. At large values of z, the lines are nearly parallel, indicating an effectively two-dimensional boundary layer on the flat plate.

The fact that the body boundary layer is indeed two-dimensional quite near the juncture is emphasized in figure 13 where the body boundary layer profiles are unchanged for $y \geq 51$ mm (≥ 2.0 in.). For this reason, it was decided to use as the two-dimensional body boundary layer profile the profile taken at $y = 76$ mm (3.0 in.) with the body mounted on the flat plate rather than making a separate measurement with the body in isolation.

Figures 12 and 13 also reflect the precision of the surveys when it is recognized that the nearly parallel lines for small z in figure 12 and the profiles in figure 13 were obtained by moving the hot wire over large distances parallel to the body surface at varying values of z.

Extrapolation of Mean Velocity Profiles

In order to evaluate the total momentum deficit in the juncture, it is necessary to know the value of U_x over the entire rectangular area of integration. In particular, U_x must be measured from the outer edges of the rectangle to the surfaces at $y = 0$ and $z = 0$. Because of the physical size of the horizontal hot-wire probes used here, the minimum height that the sensor could be placed above the flat plate was $y = 0.50$ mm (0.02 in.) and the minimum distance that the sensor could be located away from the body surface was $z = 2.5$ mm (0.10 in.). Therefore, the measured data were extrapolated to $y = 0$ and $z = 0$ by appealing to the Law of the Wall for two-dimensional turbulent boundary layers (figs. 14, 15).

In figure 14, the measured values of U_x at the smallest possible value of y, namely $y = 0.50$ mm (0.02 in.), for each transverse, z, measuring station were made to coincide with the straight line representing the Law of the Wall by selecting the shear velocity, U_τ. Having determined U_τ, all of the measurements at larger values of y were

plotted as shown in figure 14. For intermediate values of y the data follow the Law of the Wall, as noted earlier by Shabaka (refs. 15, 16). At large values of y the measured data diverge from the straight line. For large values of z the plate boundary layer flow is nearly two-dimensional so the curves for large y in figure 14 are slightly above the straight line and exhibit the expected "wake-like" behavior. At very small values of z the measured velocity profiles in y are completely within the body boundary layer so that on the plot of figure 14 the curves at large y fall below the straight line. At intermediate values of z, near the secondary flow core, the curves for large y overshoot the straight line by a considerable amount.

With the Law of the Wall verified for intermediate values of y, the plot of figure 14 was used to extrapolate downward in y to obtain new values of U_x. This extrapolation was continued until $yU_\tau / \nu = 5$ was reached, at which time a linear fit was taken between that value of U_x and $U_x = 0$ at $y = 0$ as seen by the dashed line in figure 14. These extrapolated values of U_x were used in the momentum deficit calculations.

Figure 15 was used in a similar way to extrapolate from the last measured point at $z = 2.5$ mm (0.10 in.) down to the body surface. At large values of z in figure 15, the curves which fall below the straight line are those for value of y small enough so that the entire traverse in z was within the plate boundary layer. The curves which rise above the straight line and then are flat correspond to traverses in z at sufficiently large values of y so that the traverses go through the entire body boundary layer and then into the uniform free stream at a constant value of U_x (i.e., potential flow).

The extrapolation procedure described above was used for all velocity profiles taken in the juncture even though some of the experimental data (not shown) did not follow the Law of the Wall within a small region bounded by $0 \le y \le 5$ mm and $0 \le z \le 2$ mm.

The local values of the shear velocity, U_τ, which have been determined from figures 14 and 15, can be used to evaluate wall shear stress and friction coefficient distributions. Plots of the calculated values of the skin friction coefficient on the plate surface in the juncture and on the body surface in the juncture are shown in figures 16(a) and 16(b), respectively. These results are in qualitative agreement with the measured values shown in reference 15. The skin friction on the plate is increased noticeably in the vicinity of the core of the secondary flow, while the skin friction on the body is relatively constant except very near the plate surface. Right in the corner, both surfaces experience very little friction.

Momentum Thickness

Juncture. The local momentum thickness in the juncture region is shown in figure 17 plotted against distance along the flat plate (fig. 17(a)) and distance along the body (fig. 17(b)). These momentum thicknesses are defined as

$$\theta_y = \int_0^y \frac{U_x}{U_e}\left(1 - \frac{U_x}{U_e}\right) dy \Bigg|_z \tag{24}$$

and

$$\theta_z = \int_0^z \frac{U_x}{U_e}\left(1 - \frac{U_x}{U_e}\right) dz \Bigg|_y \tag{25}$$

Referring to figure 17(a) with $z > 25$ mm (> 1.0 in.), it is seen that θ_y reaches a constant value when the edge of the viscous layer is reached. For $z < 25$ mm (< 1.0 in.) the values of θ_y continually increase as the upper limit on the integral is increased since the profiles in y are within the body boundary layer and, as larger values of y are taken in the integration , more and more of the momentum deficit in the body boundary layer is being included.

The same pattern is evident in figure 17(b). Here, for $y > 51$ mm ($y > 2.0$ in.) the velocity profiles in z go through the body boundary layer to the freestream, $U_x/U_e \to 1$, and the values of θ_z converge. For small y, the measured profiles in z are completely within the plate boundary layer so that as the upper limit, z, is increased, more and more plate boundary layer momentum deficit is included and the value of θ_z continually increases. Because the effect of the secondary flow is pronounced on the plate boundary layer (fig. 12), the plate boundary layer thickness is distorted. Hence the curves of θ_z for small y are not as linear as those for θ_y at small z. The height $y = 25$ mm (1.0 in.) represents the dividing line between velocity measurements taken with the two different hot-wire probes. This is reflected in the small irregularities in θ_z at this height on figure 17(b).

Figure 17 also indicates that at suitably large values of z and y both θ_y and θ_z become constants independent of distance away from the corner. Thus, both approach a two-dimensional condition. This is seen more clearly later in the discussion of cumulative momentum deficits.

Flat Plate. The momentum thickness of the two-dimensional boundary layer on the flat plate in the absence of the body is shown in figure 18 as a function of transverse distance, z. The flat plate only momentum thickness has been calculated from the vertical (y) profiles up to y = 94 mm (3.7 in.) that corresponds to a height above the plate which is well in the freestream flow. Thus, in figure 18 the momentum thickness plotted is

$$\theta_{y = 94} = \int_0^{94} \frac{U_x}{U_e}\left(1 - \frac{U_x}{U_e}\right) dy \Bigg|_z \tag{26}$$

Also shown in figure 18 for comparison purposes is the distribution of $\theta_{y = 94\ mm}$ versus z in the juncture flow (flat plate and body). This value of y again is sufficiently large so that all of the momentum thickness is included. Thus, the plot of $\theta_{y = 94\ mm}$ in figure 18 is the envelope of the θ_y curves in figure 17(a), where that part of the curve for small z has been omitted for clarity. The distortion of the flat plate boundary layer momentum thickness caused by the secondary flow in the juncture is apparent in figure 18.

Cumulative Momentum Deficit

The cumulative momentum deficit in the juncture is shown in figures 19 and 20. Figure 19(a) is a repeat of the momentum thickness distribution shown in figure 17(a) in the sense that it is a plot for $\theta_{y = 94\ mm}$. This particular value of y was chosen because above this height the spacing of the data-taking stations in the vertical direction became wider. Also, this value of y is sufficiently large so that this single curve in figure 19(a) represents the envelope of the curves in figure 17(a) for values of z outside the body boundary layer. At small values of z this specific choice of y selects a single curve from the many shown in figure 17(a), but this is not of concern since it is the behavior of the cumulative momentum deficit at large z that is of interest here.

For the value of y selected as in figure 19(a), the cumulative momentum deficit is given by

$$K_z = \int_0^z \theta_{y = 94}\, dz \tag{27}$$

Physically, this equation means that a line of length 94 mm perpendicular to the plate is being swept in the positive z direction from z = 0 outwards, and that the momentum thickness swept through by this line is being accumulated by integration to yield a momentum area (i.e., the area in the freestream through which the momentum flow rate is equal to the momentum deficit). The resulting cumulative momentum deficit, K_z, is plotted as a function of the swept distance, z, in figure 19(b). The value of the ordinate in this figure at any z thus represents the area under the curve in figure 19(a) from z = 0 out to that same z.

Of particular interest here is the behavior of both curves in figure 19 for large z. Figure 19(a) shows that the values of $\theta_{y = 94\ mm}$ approaches a constant as z approaches 152 mm (6.0 in.). Figure 19(b) shows a linear relation between K_z and z for large z, with a slope which agrees with the value of $\theta_{y = 94\ mm}$ at z = 152 mm (6.0 in.) to within 1%. The significance of this is that the boundary layer on the flat plate is essentially two-dimensional when this value of z is reached, as noted earlier. Thus, if the total momentum deficit, or momentum area (i.e., $0 < y < 94$ mm and $0 < z < 152$ mm), in the juncture is calculated over a rectangle having a dimension in z of 152 mm (6.0 in.) then all of the momentum deficit due to the juncture flow will have been accounted for in this direction. A rectangle with a larger z dimension would simply add an increment of a two-dimensional boundary layer to the juncture total momentum deficit.

Another indication that the three-dimensional juncture flow is essentially two-dimensional at z = 152 mm (6.0 in.) is seen in figure 18. Note that the juncture flow curve for $\theta_{y = 94\ mm}$ asymptotically approaches the value for the flat plate boundary layer as z approaches its outer limit. This behavior also supports the validity of the pressure correction approach used here. That is, the momentum thickness obtained from the velocity profile which had been adjusted to the static pressure level existing in the freestream above the flat plate agrees with the momentum thickness measured for the flat plate boundary layer in isolation.

Figure 20 presents the same information for the body boundary layer as did figure 19 for the flat plate boundary layer. Figure 20(a) is a repeat of the envelope (at least for larger z) of the curves in figure 17(b) with z = 152 mm (6.0 in.). Thus,

$$\theta_{z = 152} = \int_0^{152} \frac{U_x}{U_e}\left(1 - \frac{U_x}{U_e}\right) dz \Bigg|_y \qquad (28)$$

For this selected value of z, a horizontal line then is swept vertically upward in y between z = 0 and z = 152 and the momentum deficit is accumulated by integration as before. Thus,

$$K_y = \int_0^y \theta_{z = 152} \, dy \tag{29}$$

The result is shown in figure 20(b). Both of the plots in figure 20 indicate that the body boundary layer becomes two-dimensional quite near the corner, and certainly by y = 76 mm (3.0 in.). Again, the behavior of K_y with y is linear at suitably large y, with a slope equal to the value of $\theta_{z = 152 \text{ mm}}$ at y = 76 mm (3.0 in.). This confirms that the total momentum deficit, or momentum area (i.e., $0 < y < 76$ mm and $0 < z < 152$ mm), in the juncture may be calculated over a rectangle having a height dimension of y = 76 mm (3.0 in.) with confidence that all of the momentum deficit in the juncture has been included.

Figures 13 and 20 show that the momentum deficit due to the two-dimensional boundary layer on the body in isolation may in fact be taken from the juncture data for $y \geq 76$ mm (3.0 in.), thus avoiding the necessity of having to test the body separately. This was the method used. The value of $\theta_{z = 152}$ at y = 76 mm was taken as the body two-dimensional boundary layer momentum thickness and was multiplied by the linear dimension 76 mm (3.0 in.) in order to obtain the total momentum deficit (i.e., momentum area) due to the body alone. In retrospect, the same procedure could have been used in evaluating the total momentum deficit due to the plate boundary layer, using as a two-dimensional value the momentum thickness $\theta_{y = 94 \text{ mm}}$ and the linear dimension 152 mm (6.0 in.). However, since the data for the flat plate alone had to be taken in order to verify the behavior noted in figure 18, it was decided to use the flat plate experimental results for the total momentum deficit due to the flat plate in isolation. As will be seen in the next section, both approaches lead to virtually the same result.

Total Momentum Deficit

The total momentum deficit, or the momentum area, for each of the three flow regimes was calculated as follows.

Juncture. The total momentum deficit in the juncture was evaluated from the experimental data using the equation

$$T_J = 2q_e \int_0^{152} \int_0^{76} \frac{U_x}{U_e} \left(1 - \frac{U_x}{U_e}\right) dydz \tag{30}$$

where the upper limits establish the size of the rectangular area in millimeters (i.e., 6.0 in. x 3.0 in.) as measured from the plate and body surfaces. These limits are somewhat arbitrary, but were taken at values which are large enough to ensure that all of the momentum deficit due to the juncture was included. The numerical value of the integral is

$$T_J = 0.236 \text{ N} \tag{31}$$

Plate. The total momentum deficit due to the flat plate was evaluated from the experimental data taken with the plate in isolation using the equation

$$T_P = 2q_e \int_0^{152} \int_0^{76} \frac{U_x}{U_e} \left(1 - \frac{U_x}{U_e}\right) dydz \tag{32}$$

where the upper limit for y has been made sufficiently large so as to include all of the momentum deficit and the limits for z are the same as in equation (30) for the juncture flow. The numerical value of the integral is

$$T_P = 0.191 \text{ N} \tag{33}$$

Body. The total momentum deficit for the body boundary layer alone was calculated from the measured value of $\theta_{z = 152}$ at y = 76 mm and the equation

$$T_B = 2q_e \cdot (76) \cdot \theta_{z = 152} = 2q_e \cdot (76) \cdot \int_0^{152} \frac{U_x}{U_e} \left(1 - \frac{U_x}{U_e}\right) dz \Bigg|_{y = 76} \tag{34}$$

This expression uses the same limits for y as in equation (30) for the juncture flow. The numerical value of the integral is

$$T_B = 0.052 \text{ N} \tag{35}$$

Interference Drag

The interference drag has been defined earlier and is the difference between the drag in the juncture and the drag due to the boundary layers on the plate and body in isolation. If the interference drag is expressed as a ratio of the combined drags of the plate and body, the interference drag may be written in terms of the quantities evaluated in this experiment as

$$D_{int} = \frac{\Delta T}{T_P + T_B} = \frac{T_J - (T_P + T_B)}{T_P + T_B} \tag{36}$$

Using the numerical values derived in the previous section,

$$D_{int} = -0.03 \text{ or } -3\% \tag{37}$$

The negative sign indicates that the effect of the interference is to reduce the drag, that is, there is a favorable interference.

The magnitude of the interference drag expressed by equation (36) decreases with an increase in the area of the rectangle over which the total momentum deficit is evaluated. This is because, as the area is increased, both T_J and $(T_P + T_B)$ increase the same amount which corresponds to the addition of more two-dimensional boundary layer on the plate and/or body. Thus, the numerator in equation (36) remains constant while the denominator increases. For example, for a rectangle from $0 < y < 152$ mm and from $0 < z < 304$ mm the value of D_{int} decreases to -1.5%.

The value of $D_{int} = -0.03$ as expressed in equation (37) has been determined by using an approximate data reduction procedure, as outlined in Appendix A. An estimate of the resulting error indicates that the true value of D_{int} is closer to $D_{int} = -0.02$. If, for the flat plate alone, the single value of θ at station $z = 152$ mm (6.0 in.) is used in the formulation of T_P rather than the integral expression for T_P used here (eq. 32), the

value of D_{int} becomes $D_{int} = -0.022$. Also, as noted earlier in the discussion of results, one could have elected to evaluate T_P by using the value of $\theta_{z = 152\ mm}$ as measured in the juncture and then multiplying this value by the dimension $z = 152$ mm (6.0 in.) This approach results in $D_{int} = -0.011$. The important point is that D_{int} is nearly zero and its value is relatively insensitive to the method used to evaluate it.

Since the value of D_{int} as expressed in equation (37) depends upon the size of the area over which the total momentum deficit is evaluated, a more meaningful expression for the interference drag might be to relate the increment in momentum deficit due to the juncture, ΔT, to the total momentum deficit on a wing (here, the constant-thickness body) having a chord length equal to the streamwise distance from the body leading edge to the measuring station (i.e., x = 902 mm (35.5 in.)) and a span equal to the chord. Thus,

$$D_{int(w)} = \frac{\Delta T}{T_{ref}} = \frac{T_J - (T_P + T_B)}{T_{ref}} \tag{38}$$

where

$$T_{ref} = \left(\frac{902}{76}\right) T_B \tag{39}$$

There is no factor of two appearing in equation (39) to reflect the fact that the wing has two surfaces (i.e., two wetted areas) because it is postulated that each surface would have the same interference drag where it meets the fuselage (plate) and hence the numerator in equation (38) also would double. With this definition of interference drag,

$$D_{int(w)} = -0.01 \text{ or } -1\% \tag{40}$$

The experimental results as expressed in equations (37) or (40) indicate that the interference drag due to the presence of the juncture for the geometry tested here is very small, or essentially zero. Although there are energy losses associated with the streamwise vorticity in the juncture and there are also areas of increased wall shear stress, the fact that the viscous layer fills in the corner between the body and the plate apparently decreases the local wall shear stress sufficiently to compensate for these adverse effects. It must be remembered that the geometry tested was a "wing" having

an elliptical leading edge and a constant thickness. Thus, pressure gradients were absent over most of the juncture for the results given above.

Induced Drag

The total momentum deficit in the juncture, T_J, is made up of two effects. One is the deficit in streamwise momentum brought about by a reduction in the mainstream velocity through the action of viscosity. The other is the deficit in streamwise momentum represented by the conversion of some streamwise momentum into kinetic energy in the transverse (y - z) plane due to streamwise vorticity, primarily in the rolled-up vortex in the juncture which trails downstream. This streamwise vorticity induces secondary velocities U_y and U_z in a manner analogous to the tip vortices shed from a wing of finite span. The induced drag due to this effect has been evaluated as

$$I = q_e \int_0^{152} \int_0^{76} \frac{U_y^2 + U_z^2}{U_e^2} \, dydz \tag{41}$$

The fraction of the total momentum deficit in the juncture due to this secondary flow effect may be expressed as

$$\frac{I}{T_J} = \frac{q_e \int_0^{152} \int_0^{76} \frac{U_y^2 + U_z^2}{U_e^2} \, dydz}{2q_e \int_0^{152} \int_0^{76} \frac{U_x}{U_e} \left(1 - \frac{U_x}{U_e} \right) dydz} \tag{42}$$

and, from the experimental results,

$$\frac{I}{T_J} = 0.0015 \text{ or } \frac{I}{T_J} = 0.15\% \tag{43}$$

Thus, the induced drag caused by the energy loss to the secondary flow is a very small fraction of the total momentum deficit in the juncture. This is in agreement with Hawthorne (ref. 2), who concluded that the interference drag is much greater than that which would be deduced from the energy in the secondary flow alone.

CONCLUDING REMARKS

The interference drag in the juncture formed by a flat plate and a body of constant thickness having a 1.5:1 elliptical leading edge has been evaluated experimentally. The interference drag was determined by using mean velocity data taken with a hot wire and calculating the total momentum deficit (momentum area) in the juncture and also in the two-dimensional turbulent boundary layers on the flat plate and on the body. The measurements were carried out at a streamwise location 16 body widths downstream of the leading edge of the body. The following conclusions may be drawn from the experimental data.

1. The interference drag due to the juncture, defined as the difference between the total momentum deficit (momentum area) in the juncture and the sum of the deficits for the two-dimensional boundary layers on the plate and body taken separately, is -3% of that drag attributable to the two boundary layers on the plate and body each taken in isolation. The negative sign implies a favorable interference.
2. The interference drag due to the juncture is -1% of the frictional drag of a wing of constant thickness and having a chord and span equal to 16 body widths.
3. The induced drag associated with the energy loss to the secondary flow in the juncture is a small fraction (0.1%) of the drag due to the juncture.
4. The three-dimensional behavior of the juncture flow is confined to a region extending approximately 2.6 body widths along the flat plate and 0.90 body widths along the body surface perpendicular to the flat plate. Outside of this region, both the viscous layers on the plate and on the body are two-dimensional turbulent boundary layers.
5. Profiles of streamwise mean velocity component in the juncture follow the Law of the Wall over a significant region near the plate and body surfaces.
6. Gradients in static pressure are very small within the juncture region.

APPENDIX A

ERROR ANALYSIS

An assumption which greatly reduced the wind-tunnel time necessary for data-taking was made in the data reduction scheme when equation (19),

$$\frac{(E_\ell)_{0,90}}{S} = hU_s \left[1 + \frac{1}{2h} \left(\frac{U_y^2}{U_s^2} + \frac{\overline{u_y^2}}{U_s^2} \right) \right] \tag{A-1}$$

was replaced by equation (20),

$$\frac{(E_\ell)_{0,90}}{S} = hU_s^* \tag{A-2}$$

An evaluation of the possible error in neglecting the second term in the square bracket in (A-1) was carried out and is discussed here.

The total momentum deficit in the juncture is defined as

$$T_J = 2q_e \int_0^{152} \int_0^{76} \frac{U_x}{U_e} \left(1 - \frac{U_x}{U_e} \right) dydz \tag{A-3}$$

Denoting the approximate value of U_s as obtained from (A-2) as a starred quantity, then the true value of U_s as gotten from (A-1) may be written (with h assumed unity) as

$$\frac{U_s}{U_e} \approx \frac{U_s^*}{U_e} \left[1 - 0.5 \left(\frac{U_y}{U_s} \right)^2 - 0.5 \left(\frac{\overline{u_y^2}}{U_s^2} \right) \right] \tag{A-4}$$

where terms of third order and higher have been neglected. Substituting (A-4) in (A-3) and recognizing that $U_x = U_s \cos \beta$,

$$T_J = T_J^* - 2q_e \int_0^{152} \int_0^{76} \left(\frac{U_s^*}{U_e} \cos\beta\right)\left(0.5 - \frac{U_s^*}{U_e} \cos\beta\right)\left[\left(\frac{U_y}{U_s}\right)^2 + \left(\frac{\overline{u_y^2}}{U_s^2}\right)^2\right] dydz \quad \text{(A-5)}$$

where T_J^* is the approximate value of the total momentum deficit in the juncture as obtained by using (A-2) in (A-3).

Equation (A-3) is also valid for evaluating the total momentum deficit for the plate alone (T_P) and for the body alone (T_B) if the equation is modified appropriately. In the T_P expression, the integrands with respect to z for integrating from z = 0 to z = 152 are constants and the upper limit on the y integration is the appropriate two-dimensional boundary layer thickness. Similarly, in the T_B expression the integrands with respect to y from y = 0 to y = 76 are constants and the upper limit in z is the body boundary layer thickness. Assuming for the two dimensional boundary layers that U_y is negligible but $\overline{u_y^2}$ is not (Ref. 9, Fig. 21 (a)), a simplified expression for T_P and T_B may be written as T_P^* and T_B^* plus some correction terms due to $\overline{u_y^2}/U_s^2$ in a manner analogous to equation (A-5).

Finally, an expression may be written for the difference in the total momentum deficit using (A-5) and its counterparts for T_P and T_B. Thus

$$\Delta T = T_J - (T_P + T_B)$$

$$= \left[T_J^* - (T_P^* + T_B^*)\right] + \delta = \Delta T_{MEASURED} + \delta \quad \text{(A-6)}$$

where δ is the error term and

$$\delta = (\text{error for juncture}) - \left[(\text{error for plate alone}) + (\text{error for body alone})\right]$$

Each of the terms in this expression was evaluated by using "worst-case" data from reference 9, figure 21. For simplicity, the juncture region was divided into four sub-regions and within each of these a mean value of U_y and $\overline{u_y^2}$ was used. The final result is

$$\frac{\Delta T}{\Delta T_{MEASURED}} = 0.989$$

This difference of about 1% is considered to be within the overall experimental accuracy of the work. Thus, the decision to replace (A-1) by (A-2) was valid with the understanding that the actual interference drag differs from the measured value by at most 0.0087.

REFERENCES

1. Gough, M. L., "The Effect of Fillets Between Wings and Fuselages on the Drag and Propulsion Efficiency of an Airplane," NACA TN 299, 1928.

2. Hawthorne, W. R., "The Secondary Flow About Struts and Airfoils," JAS, Vol. 21, No. 9, September, 1954, pp. 588-608.

3. Ling, A. T., "Study of Secondary Flow Effects on Single Symmetrical Airfoils," M. S. Thesis, Massachusetts Institute of Technology, 1952.

4. Gersten, K., "Die Grenzschichstromung in Einer Rechtwinkligen Ecke," Z. A. M. M., Vol. 39, 1959, p. 428.

5. Gersten, K., "Corner Interference Effects," AGARD Report 299, 1959.

6. Schlichting, H., Boundary Layer Theory, 6th Edition, McGraw-Hill, New York, 1968, p. 606.

7. Hoerner, S. F., Fluid-Dynamic Drag, Hoerner Fluid Dynamics (Brick Town, N. J.), c. 1965.

8. Barber, T. J., "An Investigation of Strut-Wall Intersection Losses," AIAA JA, Vol. 15, No. 10, October, 1978, pp. 676-681.

9. McMahon, H., Hubbartt, J., and Kubendran, L., "Mean Velocities and Reynolds Stresses in a Juncture Flow," NASA CR-3605, 1982.

10. McMahon, H., Hubbartt, J., and Kubendran, L. R., "Mean Velocities and Reynolds Stresses Upstream of a Simulated Wing-Fuselage Juncture," NASA CR-3695, 1983.

11. Oguz, E. A., "An Experimental Investigation of the Turbulent Flow in the Junction of a Flat Plate and a Body of Constant Thickness," Ph.D. Thesis, Georgia Institute of Technology, 1980.

12. Jorgensen, F. E., "Directional Sensitivity of Wire and Fiber-Film Probes," DISA Information Bulletin No. 11, 1971, pp. 31-37.

13. Bryer, D. W., and Pankhurst, R. C., Pressure-Probe Methods for Determining Wind Speed and Flow Directions, Her Majesty's Printing Office, London, 1971.

14. Jones, B. M., "The Measurement of Profile Drag by the Pitot Traverse Method," R. & M. No. 1688, British A. R. C., 1936.

15. Shabaka, I. M. M. A., "Turbulent Flow in an Idealized Wing-Body Junction," Ph.D. Thesis, Imperial College, London, April, 1979.

16. Shabaka, I. M. M. A., and Bradshaw, P., "Turbulent Flow in an Idealized Wing-Body Junction," AIAA Journal, Vol. 19, No. 12, February, 1981.

TABLE 1

LOCATION OF VELOCITY MEASUREMENT STATIONS
IN THE JUNCTURE

z		y			
mm	in.	mm	in.	mm	in.
2.54*	0.1*	0.51*	0.02*	15.2	0.60
5.08*	0.2*	0.76*	0.03*	17.8	0.70
7.62	0.3	1.02*	0.04*	20.3	0.80
10.2	0.4	1.27*	0.05*	22.9	0.90
15.2	0.6	1.52*	0.06*	25.4	1.00
20.3	0.8	1.78	0.07	27.9	1.10
25.4	1.0	2.03	0.08	33.0	1.30
30.5	1.2	2.29	0.09	38.1	1.50
35.6	1.4	2.54	0.10	44.5	1.75
40.6	1.6	3.81	0.15	50.8	2.00
45.7	1.8	5.08	0.20	57.2	2.25
50.8	2.0	6.35	0.25	63.5	2.50
55.9	2.2	7.62	0.30	69.9	2.75
61.0	2.4	8.89	0.35	76.2	3.00
66.0	2.6	10.2	0.40	82.6	3.25
76.2	3.0	11.4	0.45	88.9	3.50
101.6	4.0	12.7	0.50	94.0	3.70
127.0	5.0				
152.4	6.0				

*Horizontal Wire Only.

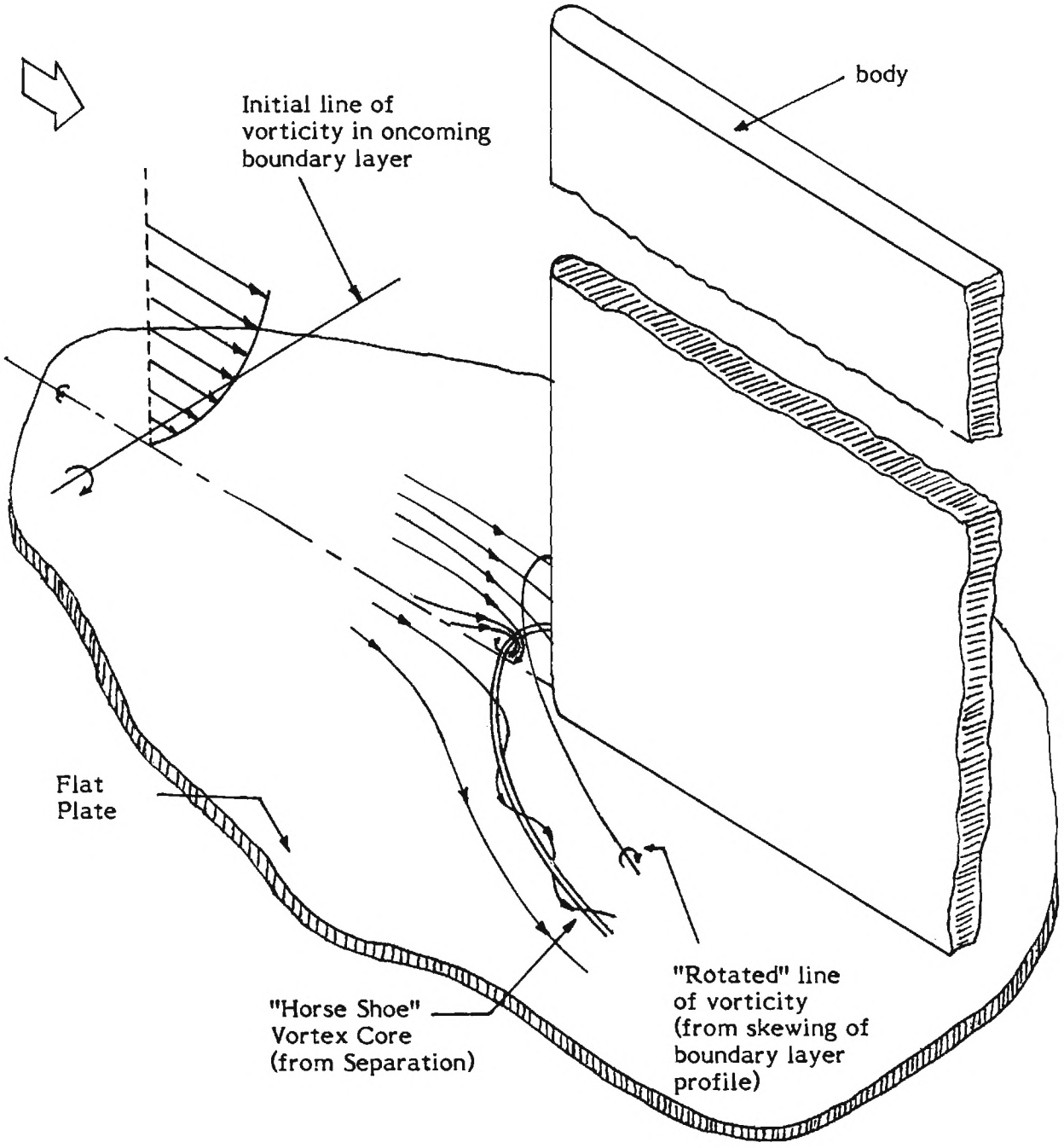

Figure 1. - Schematic of the flow in a juncture.

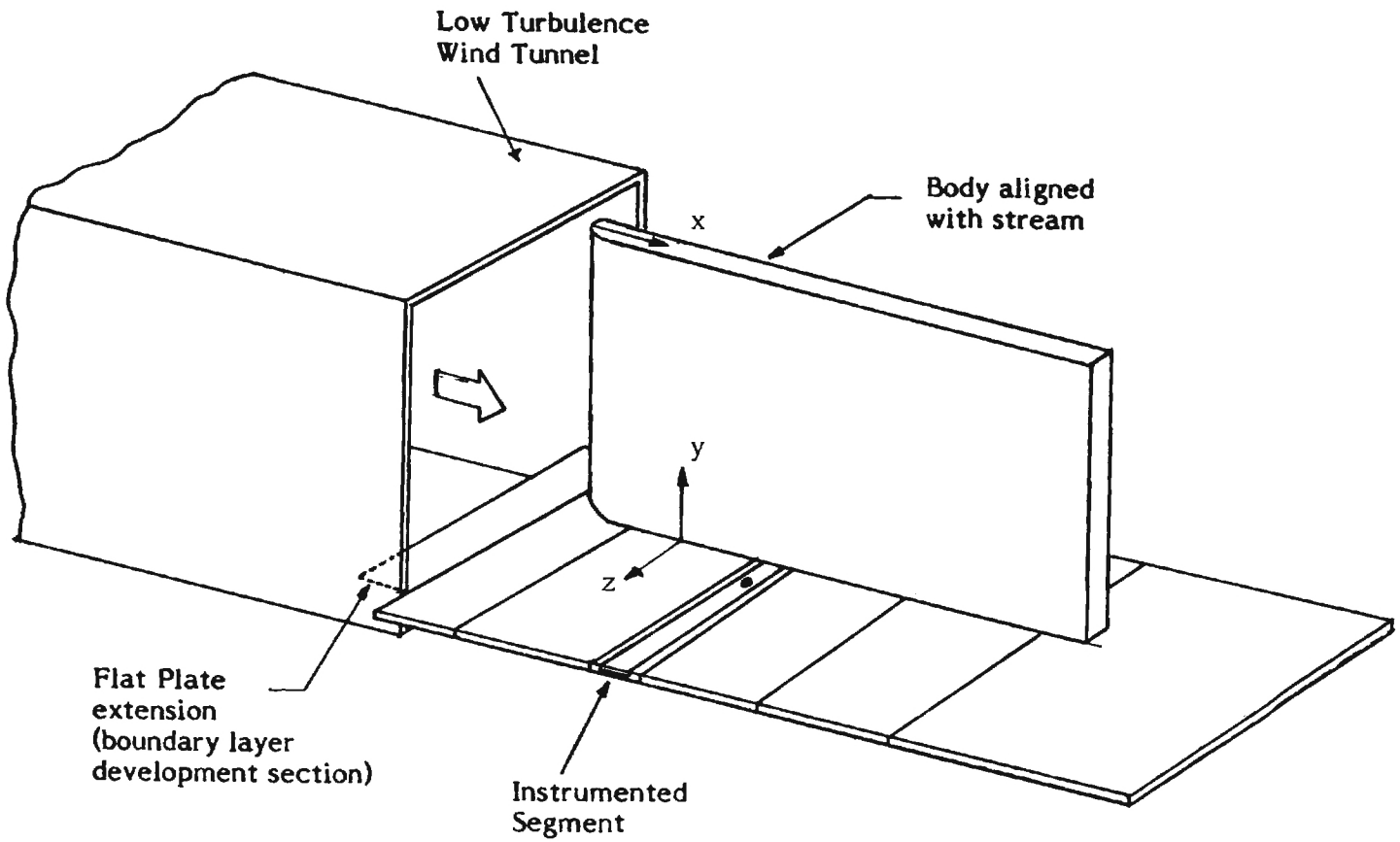

Figure 2. - Flat plate and body at the exit of the wind tunnel.

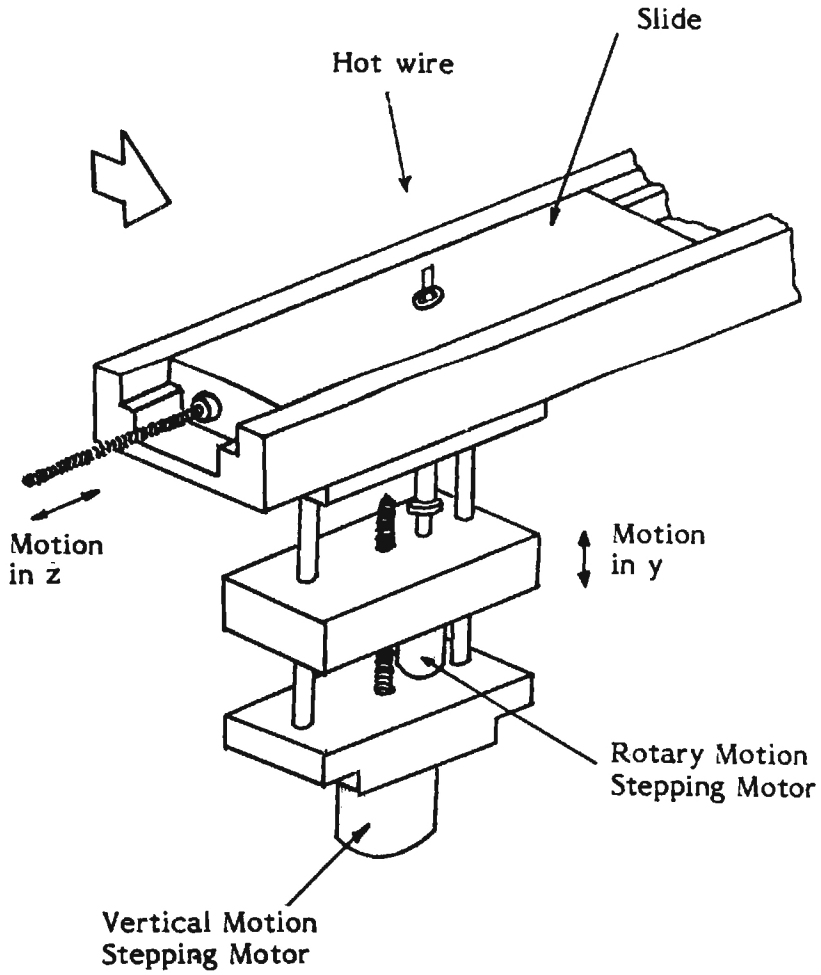

Figure 3. - Details of instrumented segment.

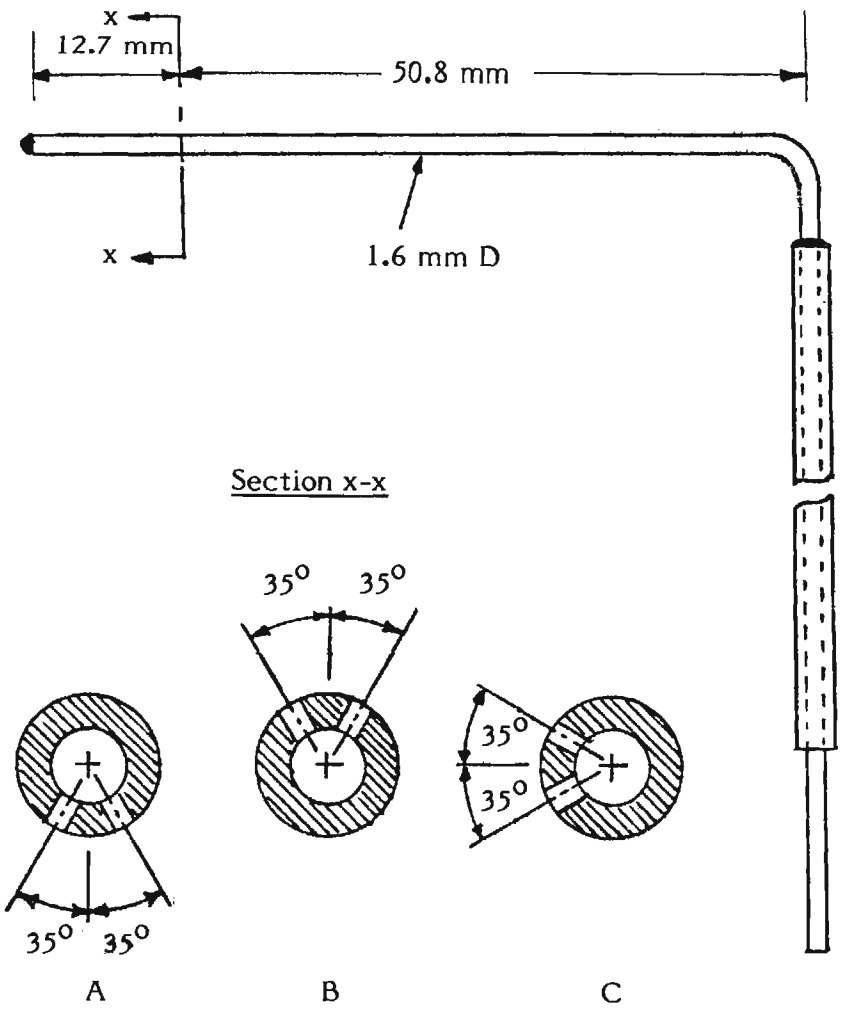

Figure 4. - Static pressure probes.

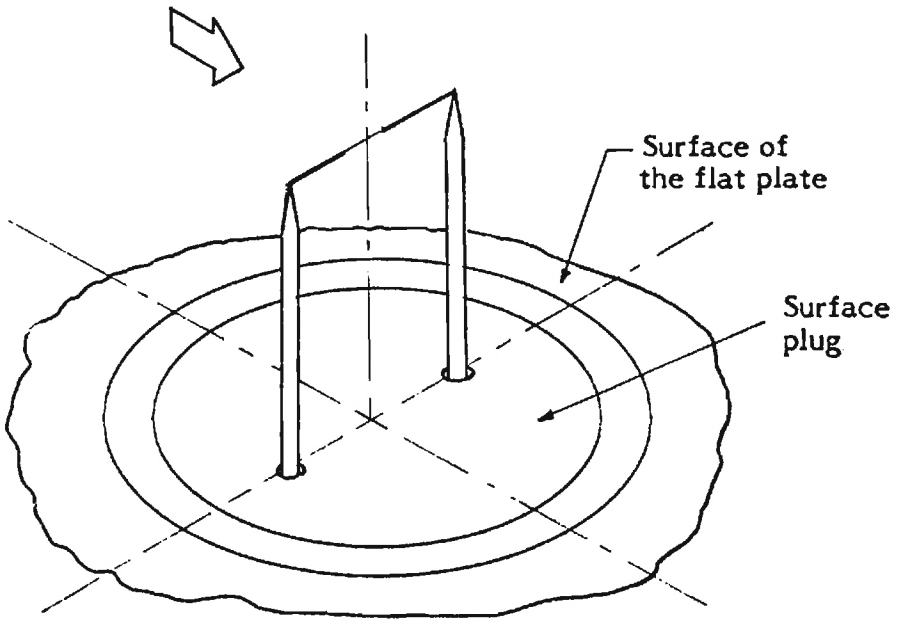

(a) Horizontal wire.

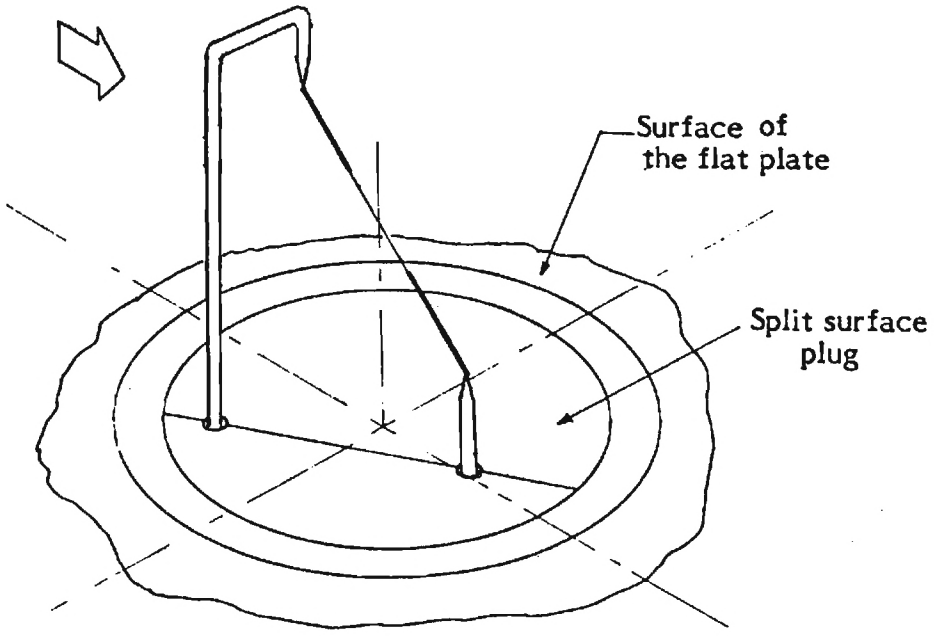

(b) Slant wire.

Figure 5. - Details of hot wires.

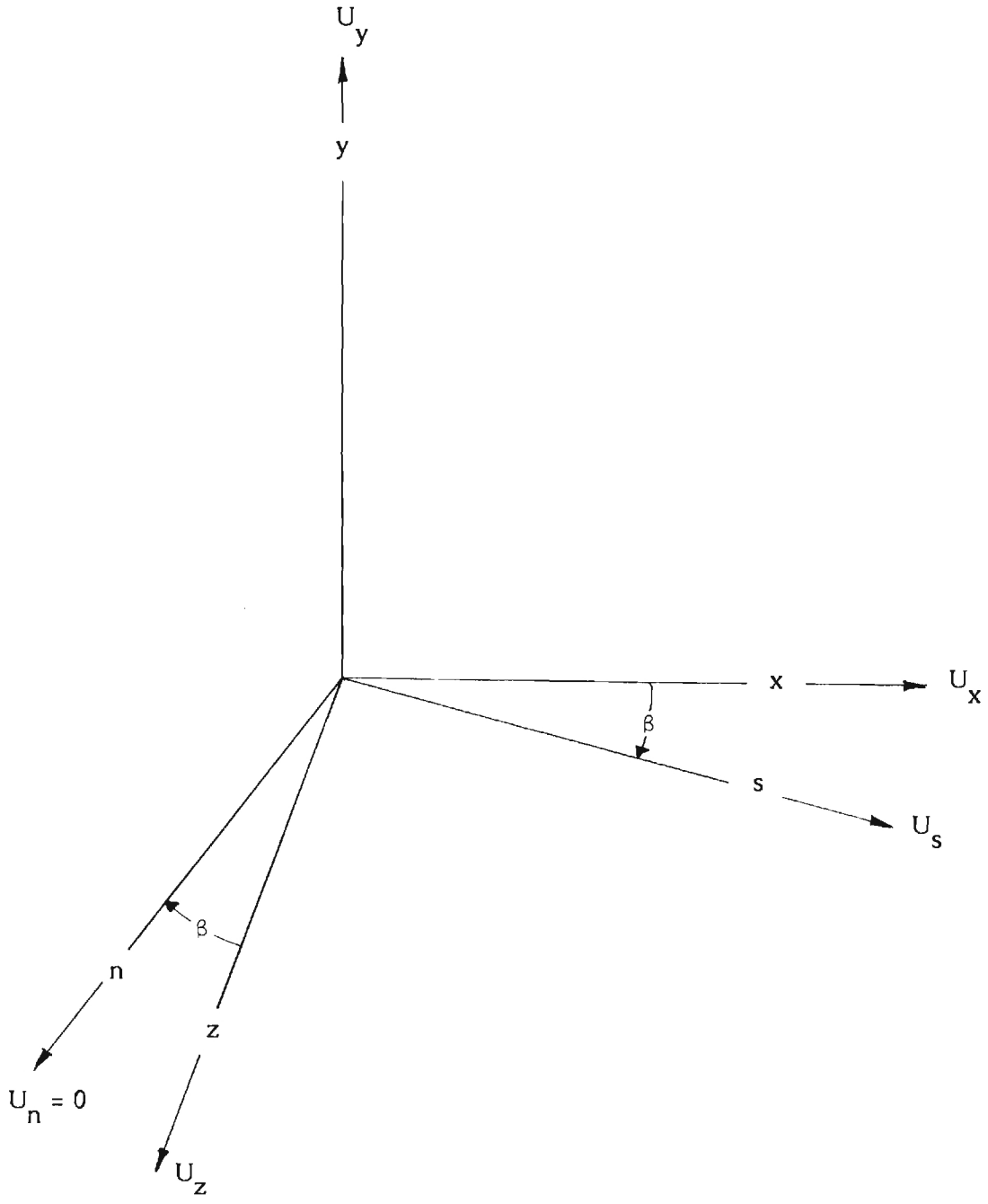

Figure 6. - The two Cartesian co-ordinate systems.

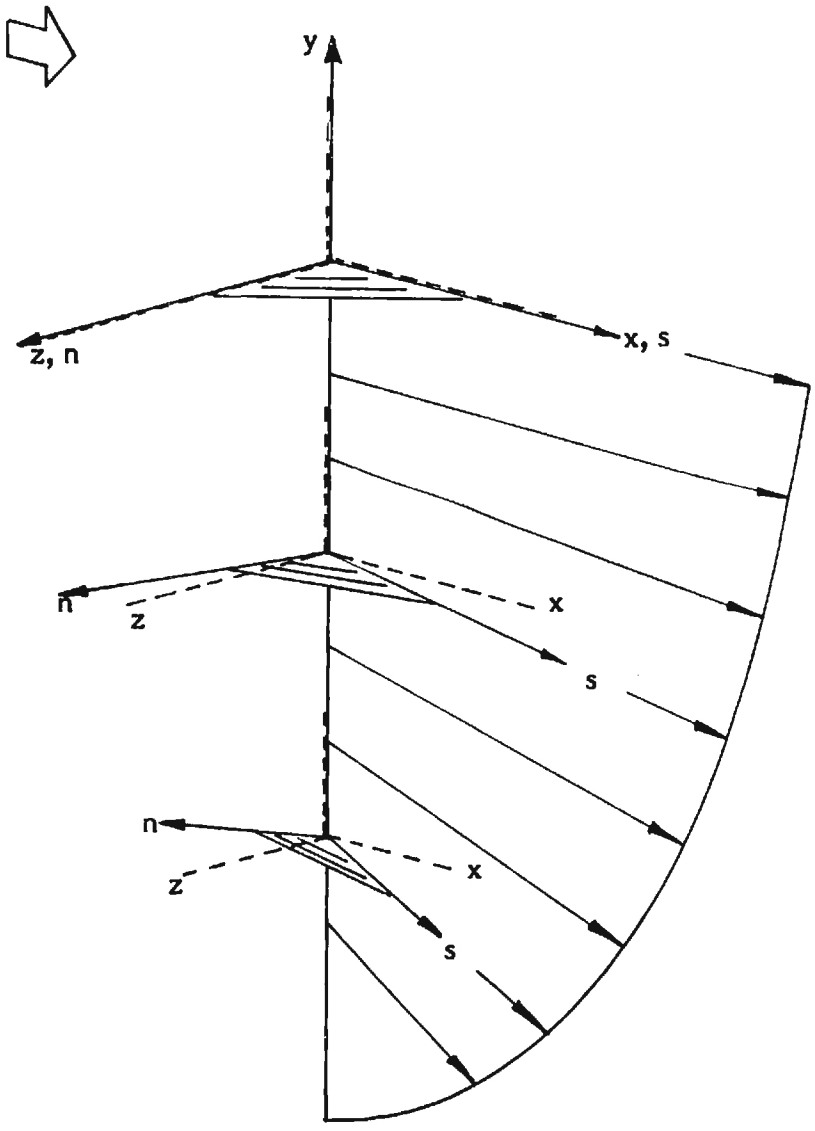

Figure 7. - Coordinate axes.

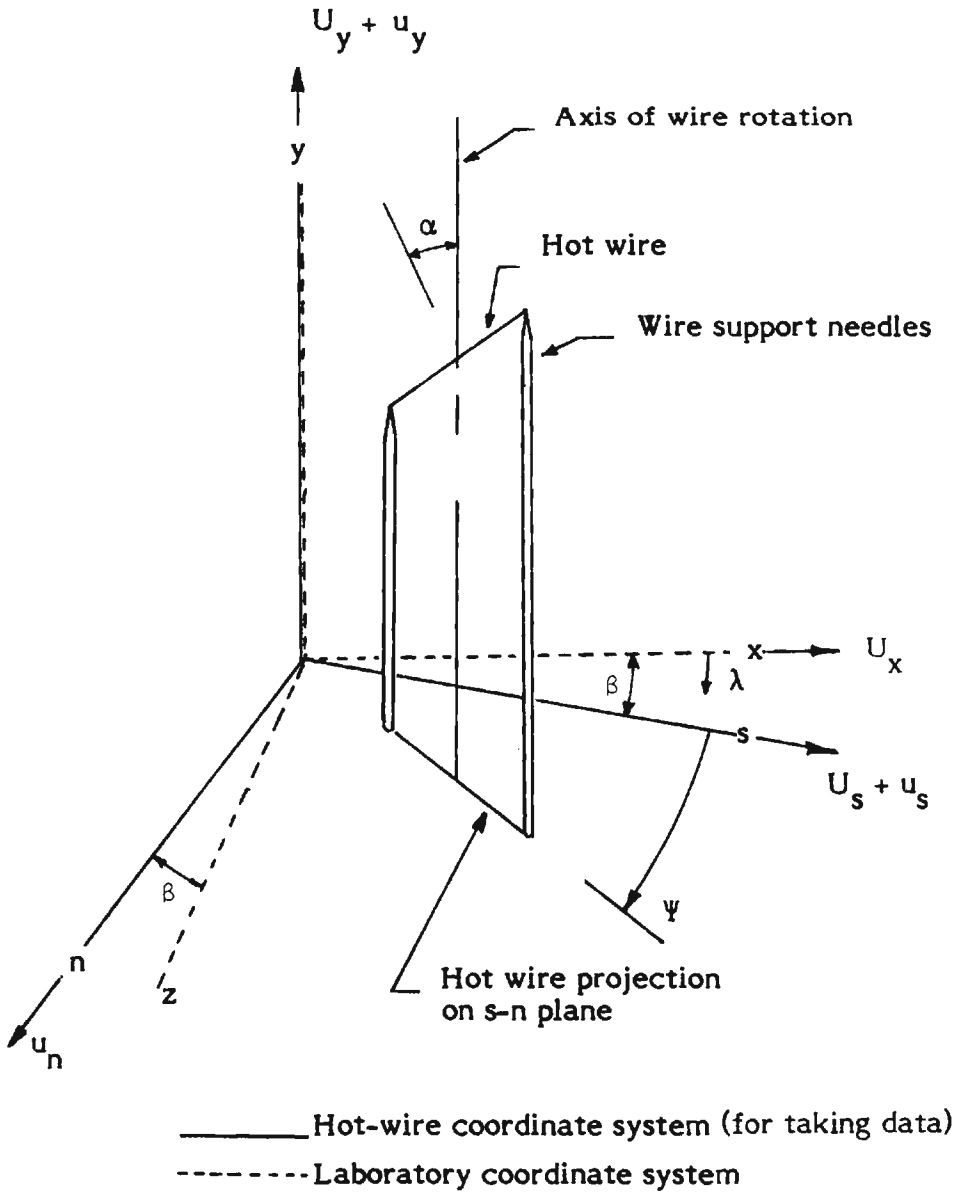

Figure 8. - Schematic of hot wire in the Cartesian coordinate system.

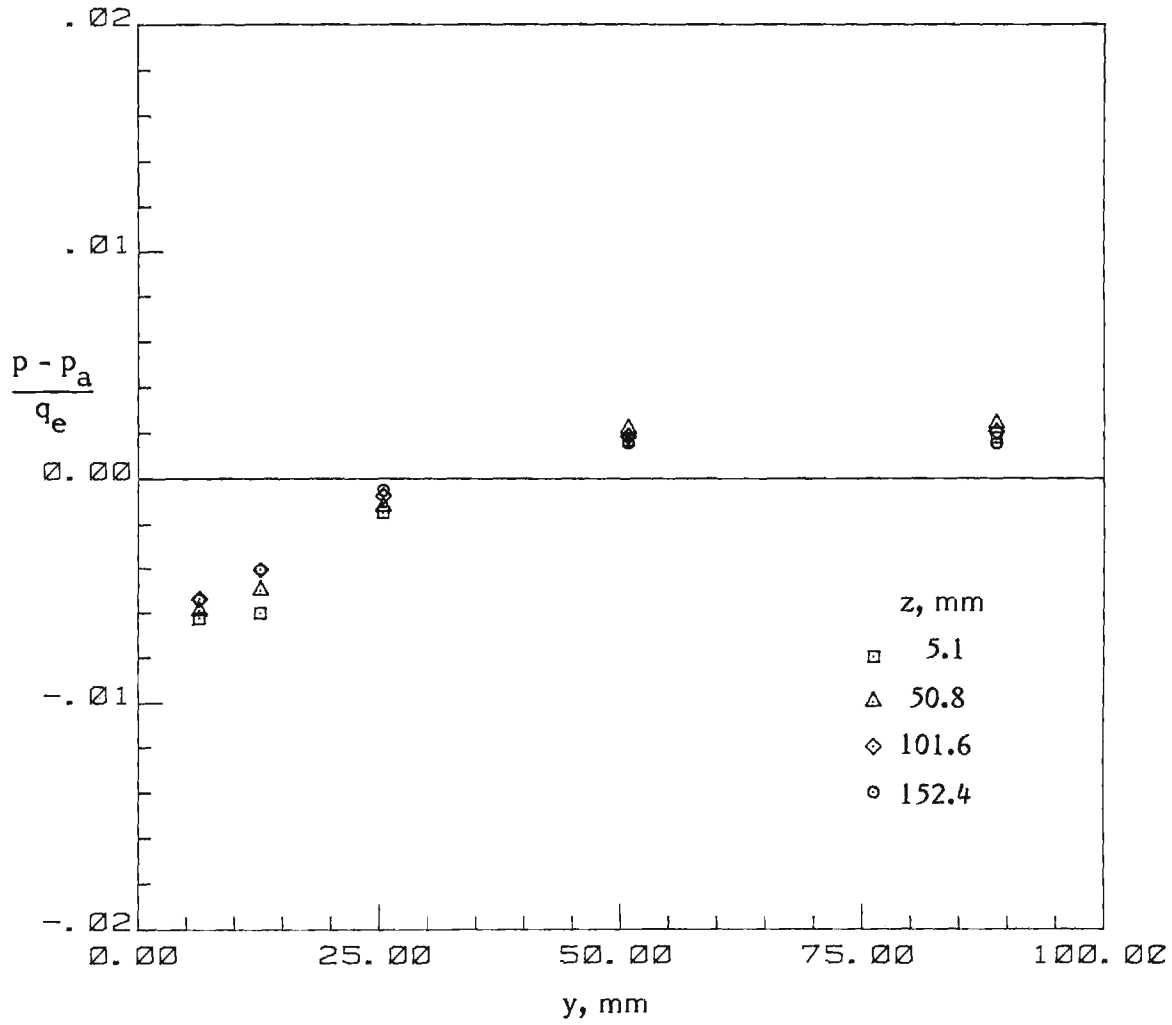

Figure 9. - Static pressure variation through flat plate boundary layer.

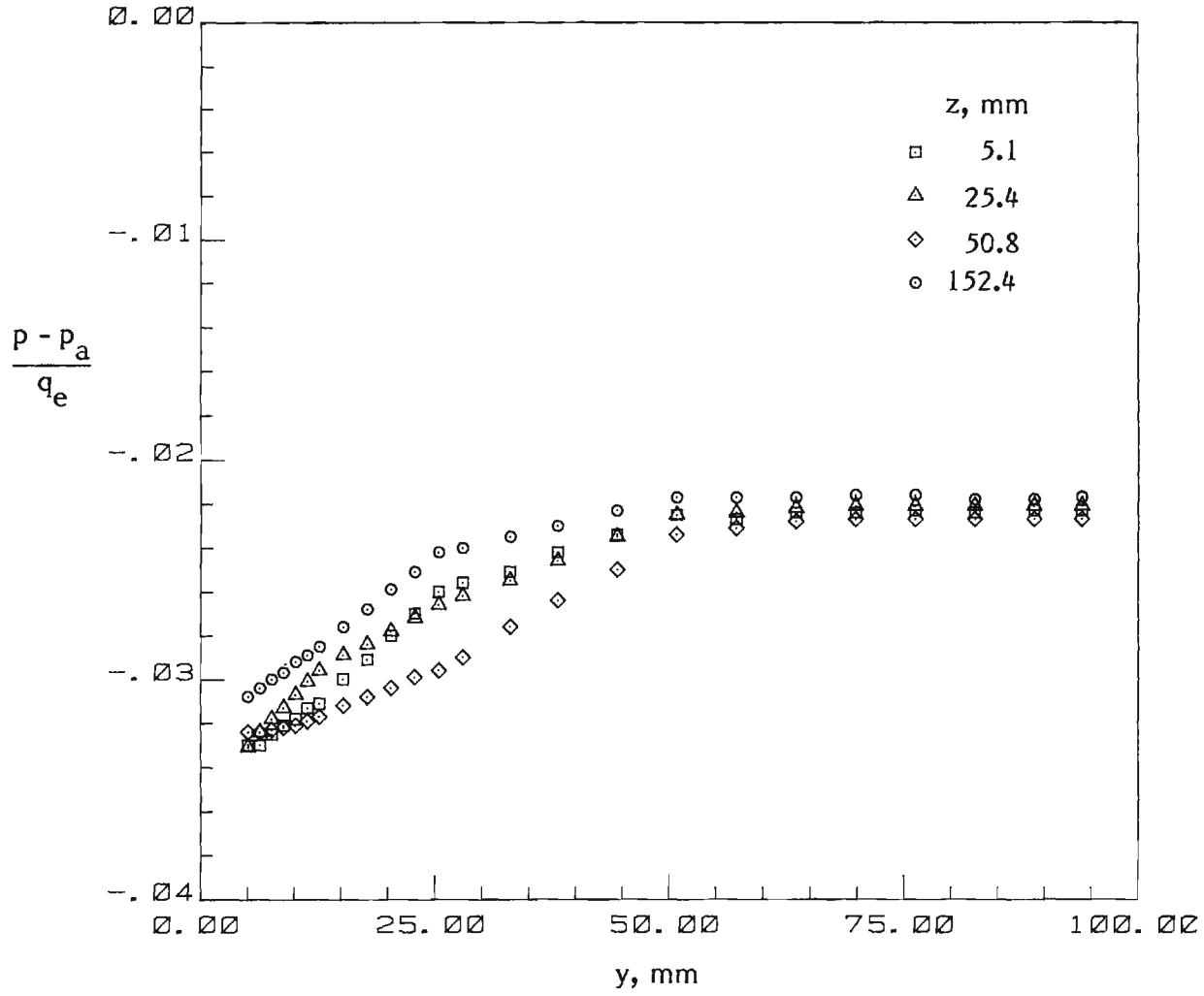

Figure 10. - Static pressure surveys in juncture.

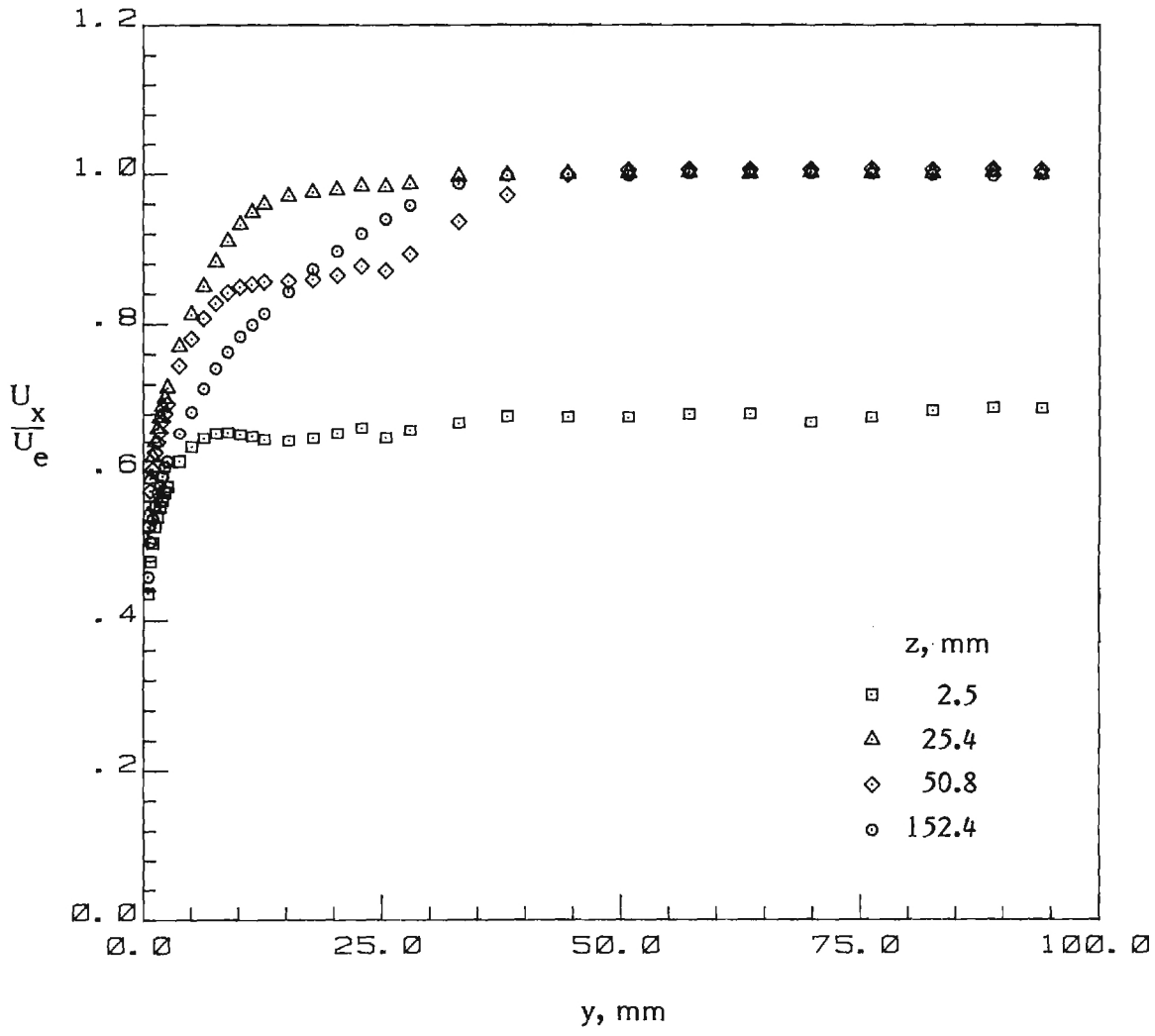

Figure 11. - Mean velocity profiles on flat plate in juncture.

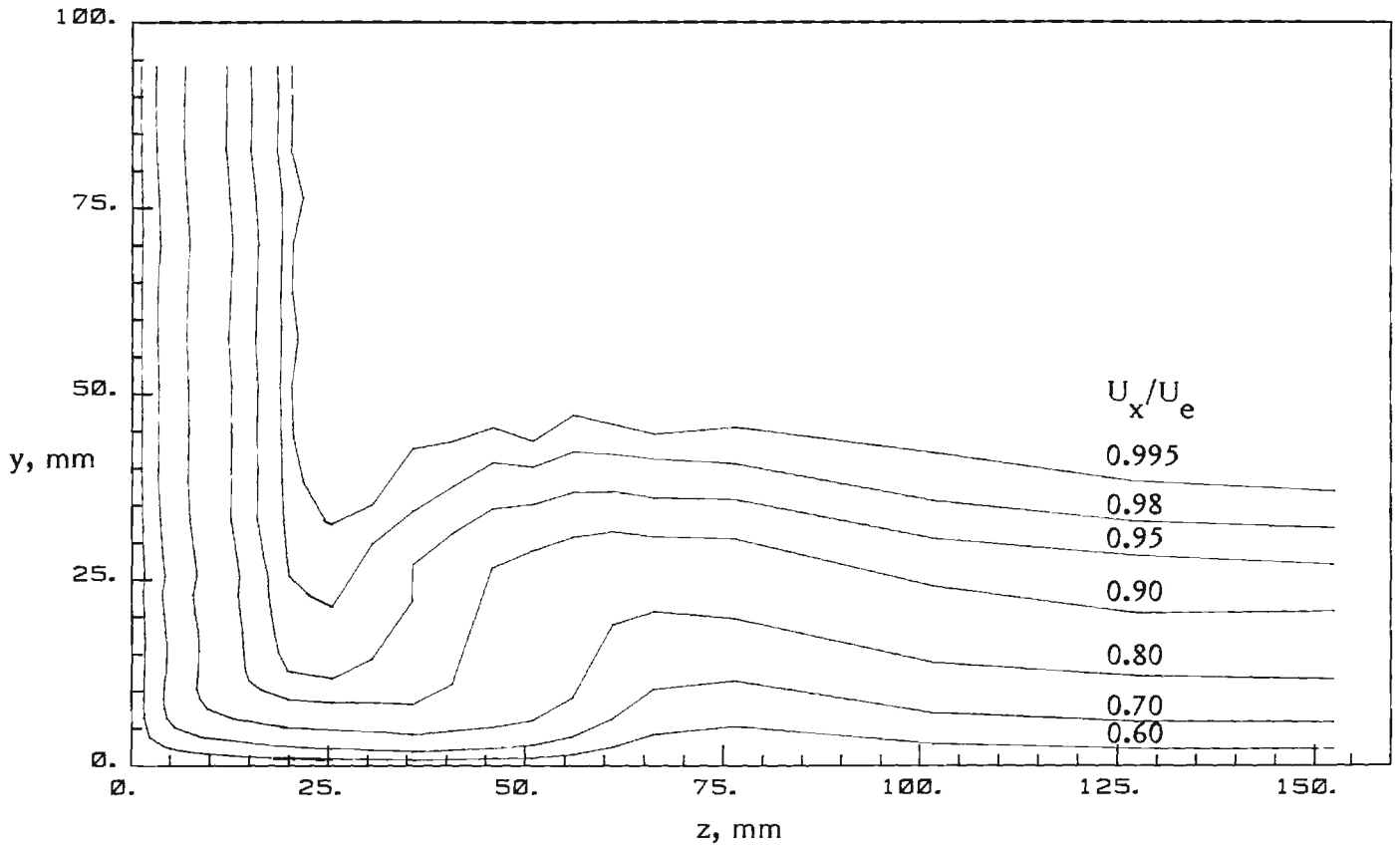

Figure 12. - Contour plots of mean velocity component U_x.

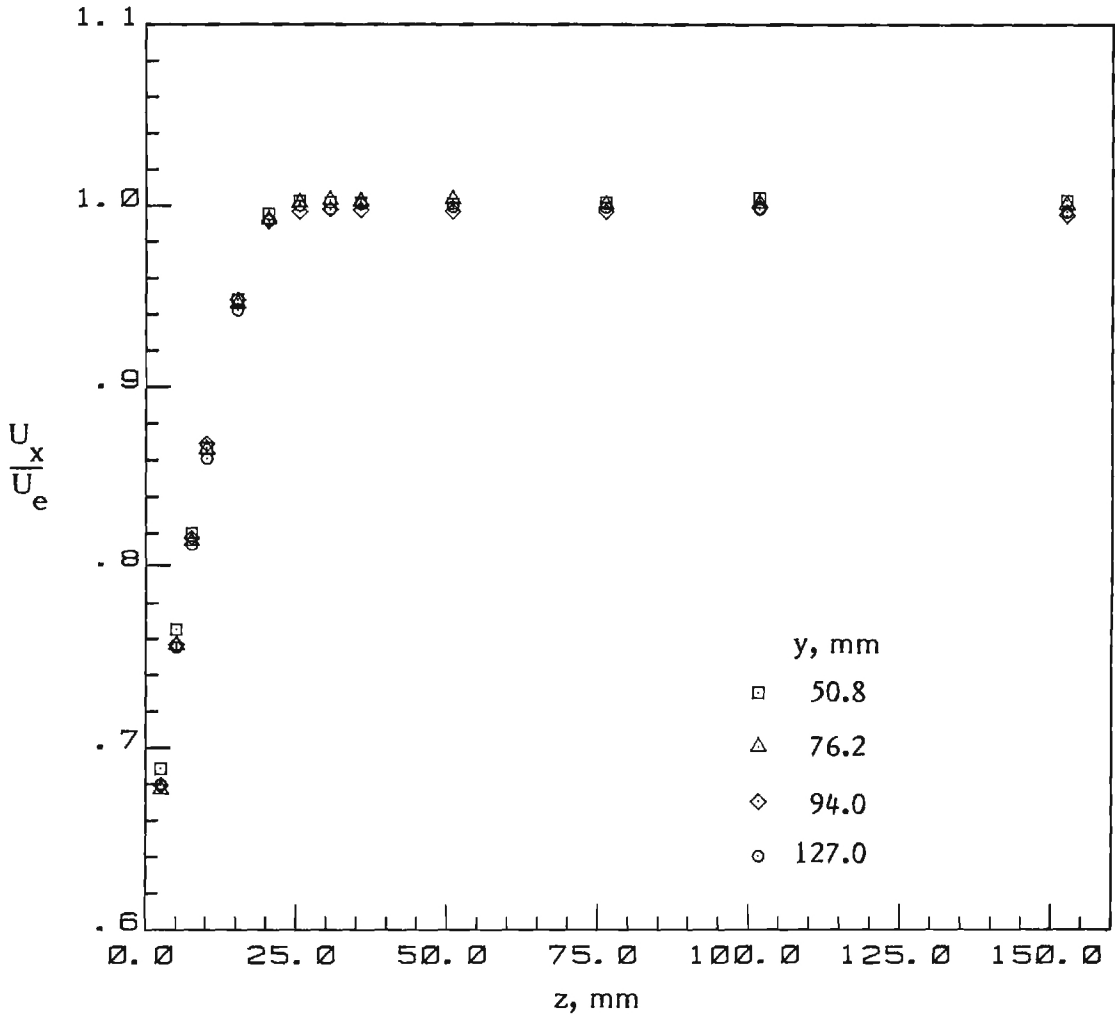

Figure 13. - Mean velocity profiles on body in juncture.

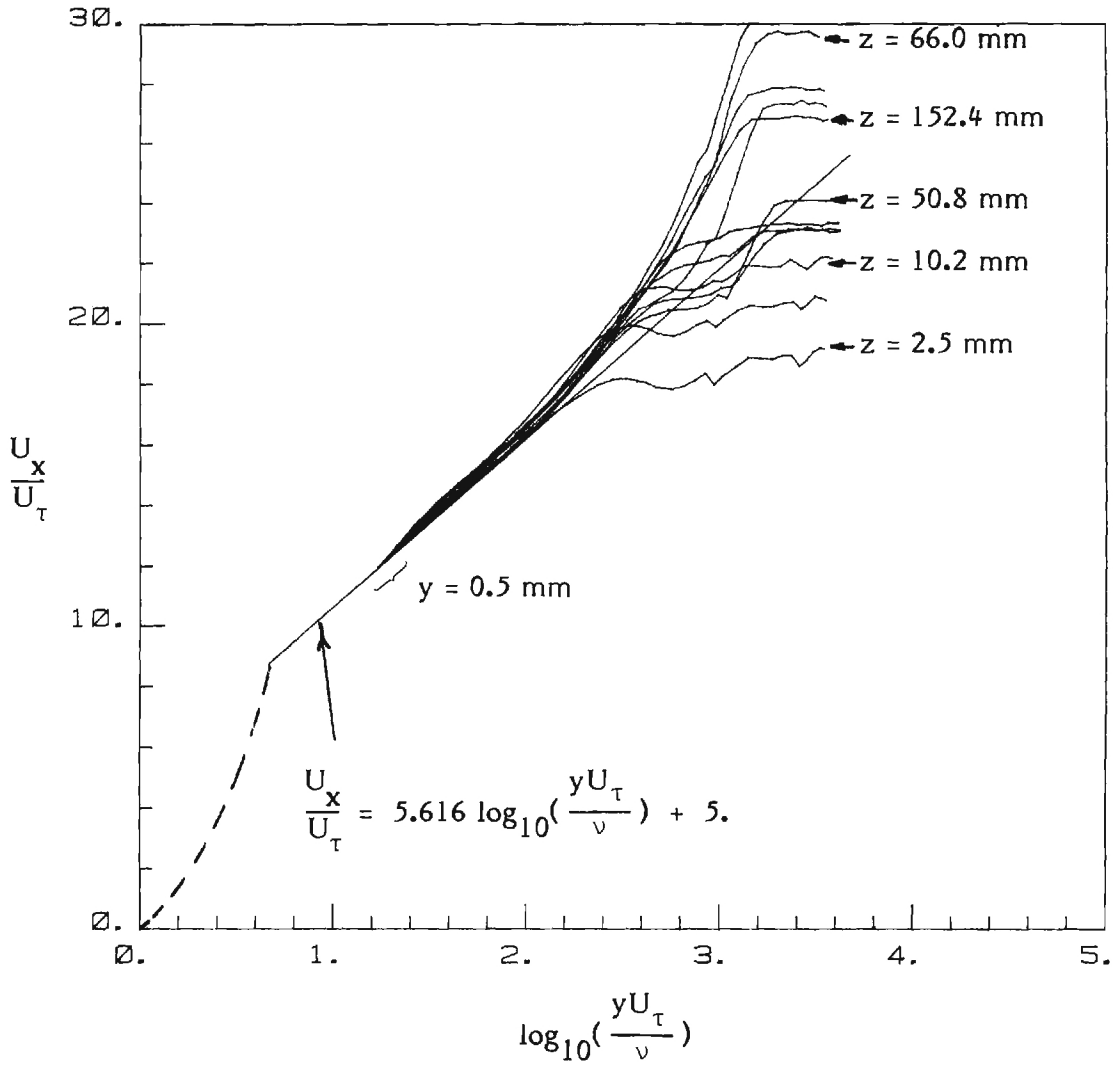

Figure 14. - The law of the wall for flat plate profiles of U_x in the juncture.

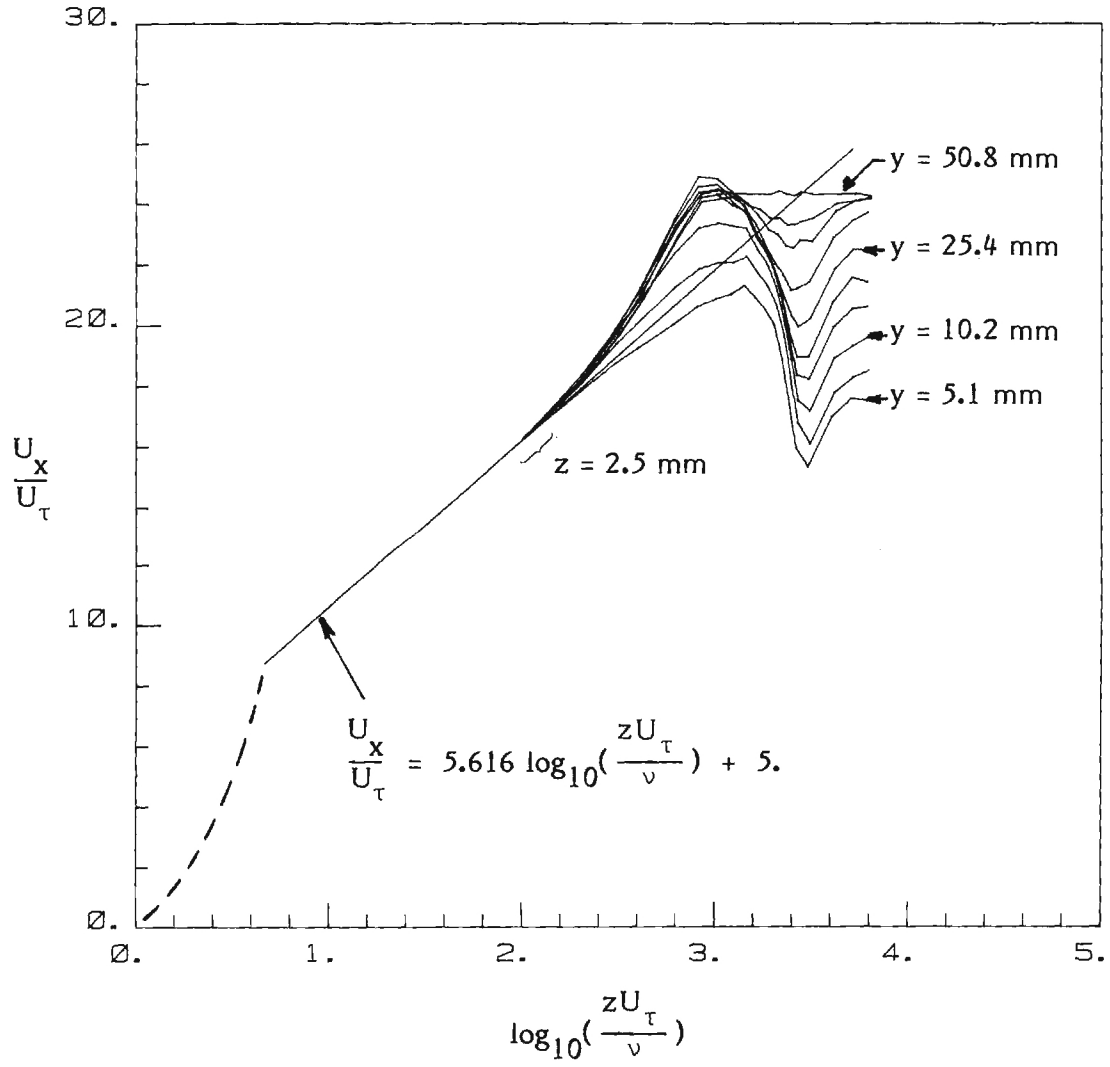

Figure 15. - The law of the wall for body profiles of U_x in the juncture.

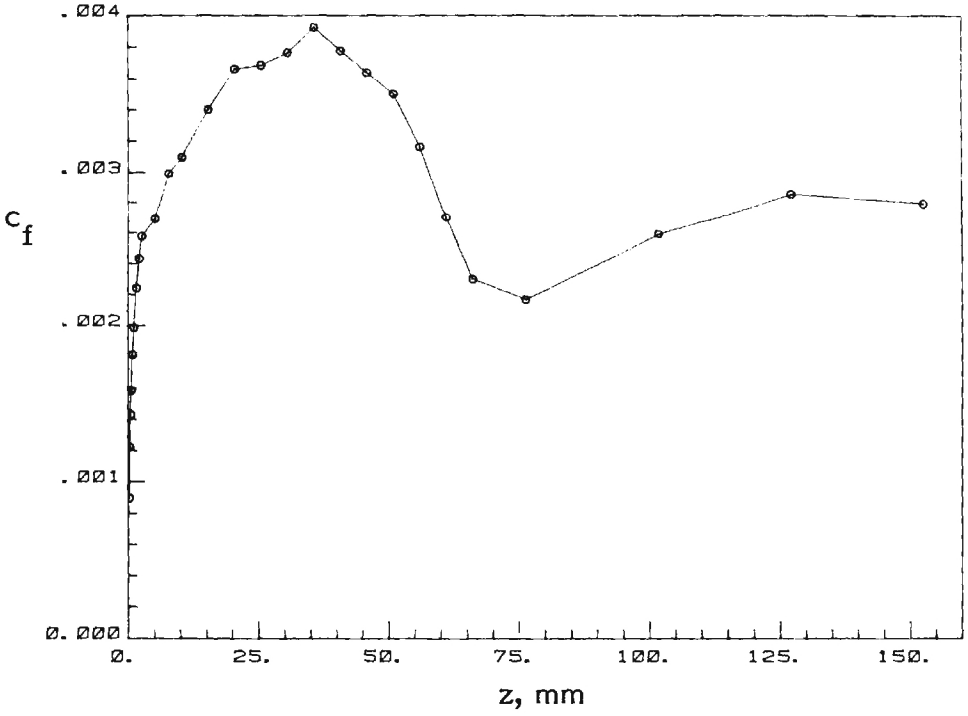

(a) Plate surface

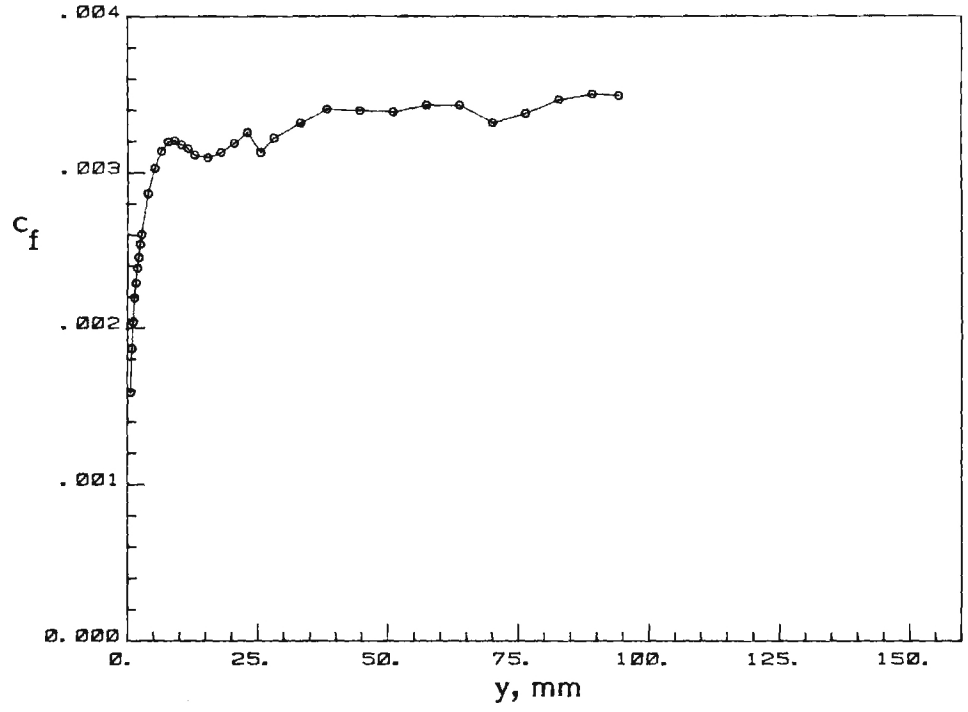

(b) Body surface

Figure 16. - Calculated values of skin friction coefficient in the juncture.

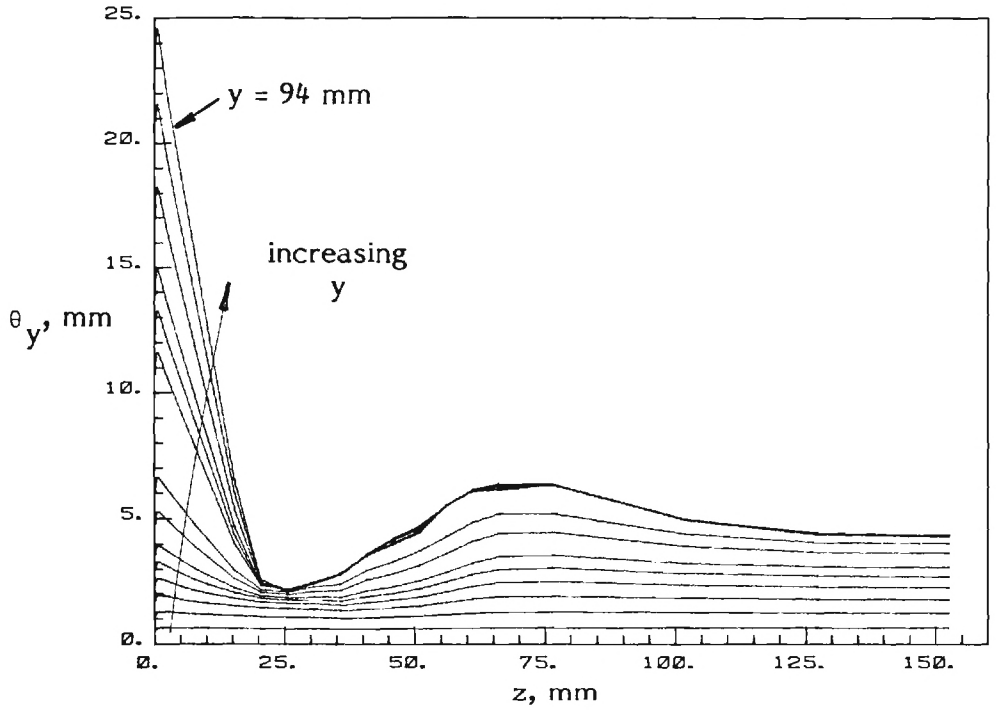

(a) Along the plate surface.

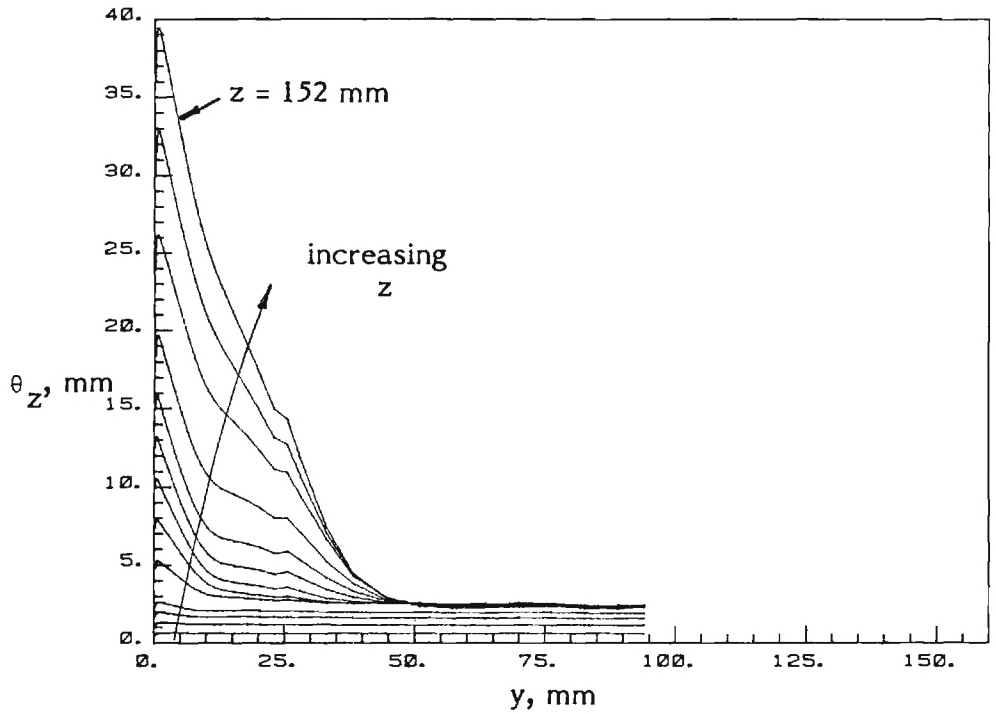

(b) Along the body surface.

Figure 17. - Momentum thickness distribution in the juncture.

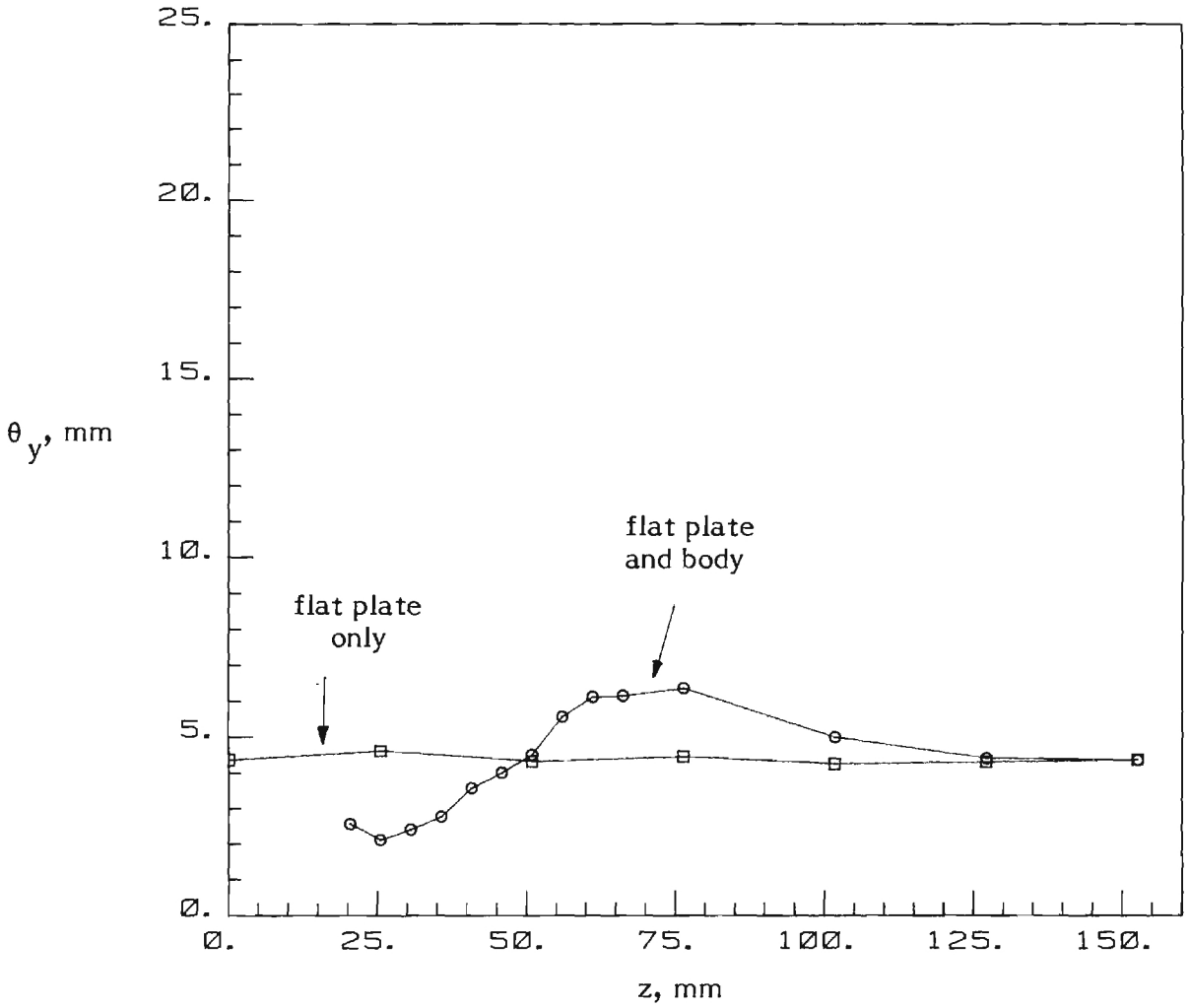

Figure 18. - Momentum thickness distribution along the plate surface with and without the body (y = 94 mm).

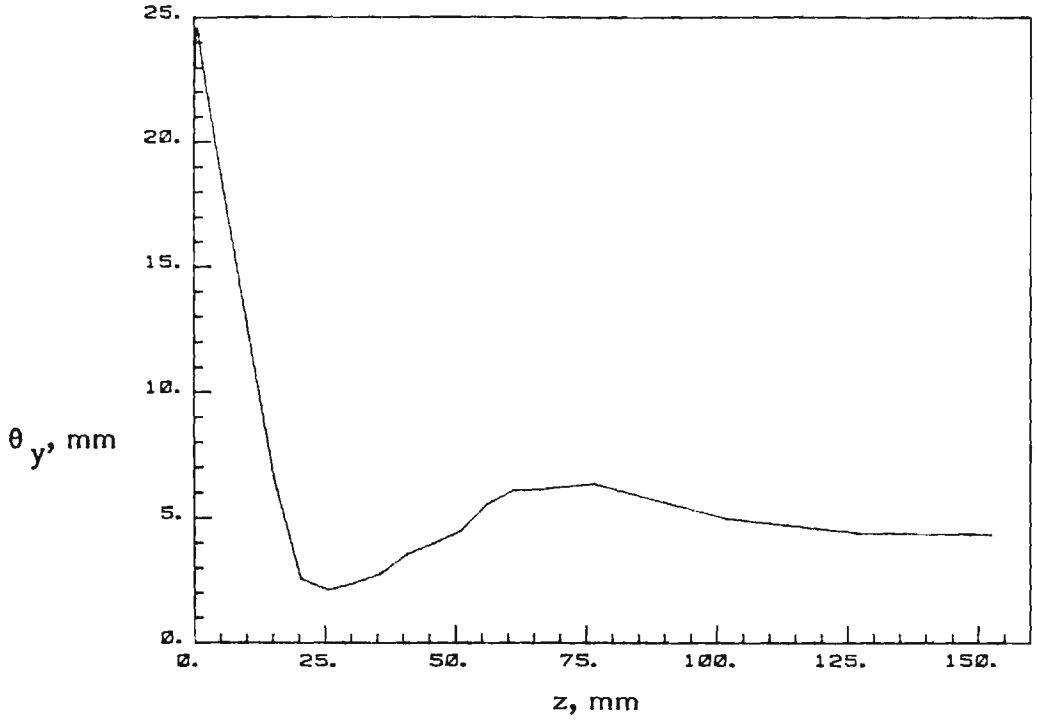

(a) Momentum thickness distribution (y = 94 mm)

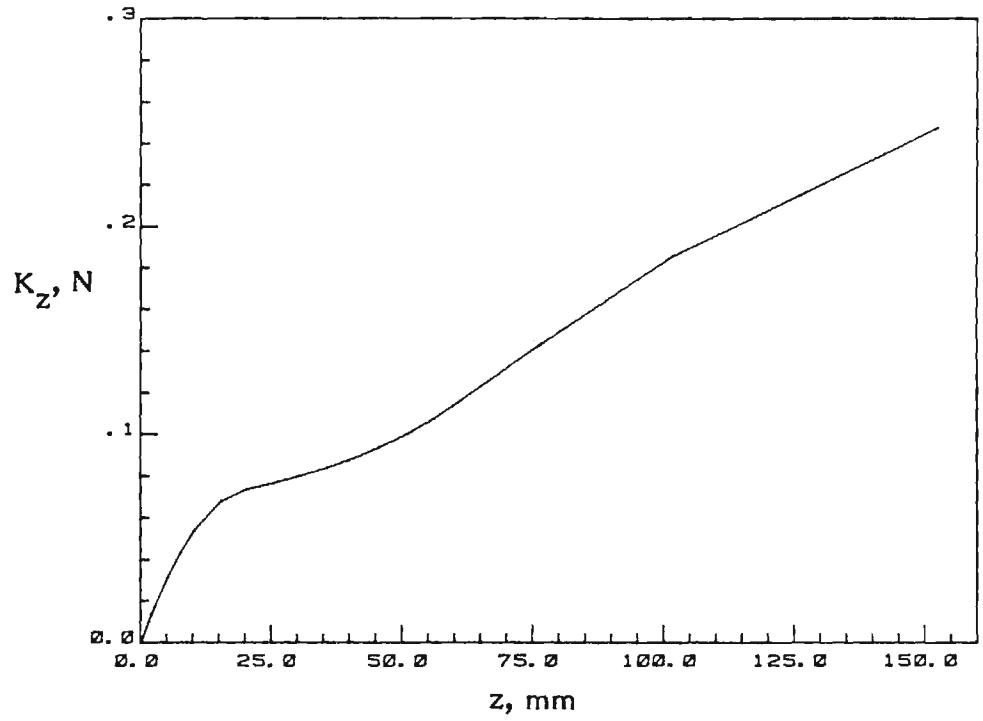

(b) Cumulative momentum deficit.

Figure 19. - Momentum thickness and cumulative momentum deficit along plate in juncture.

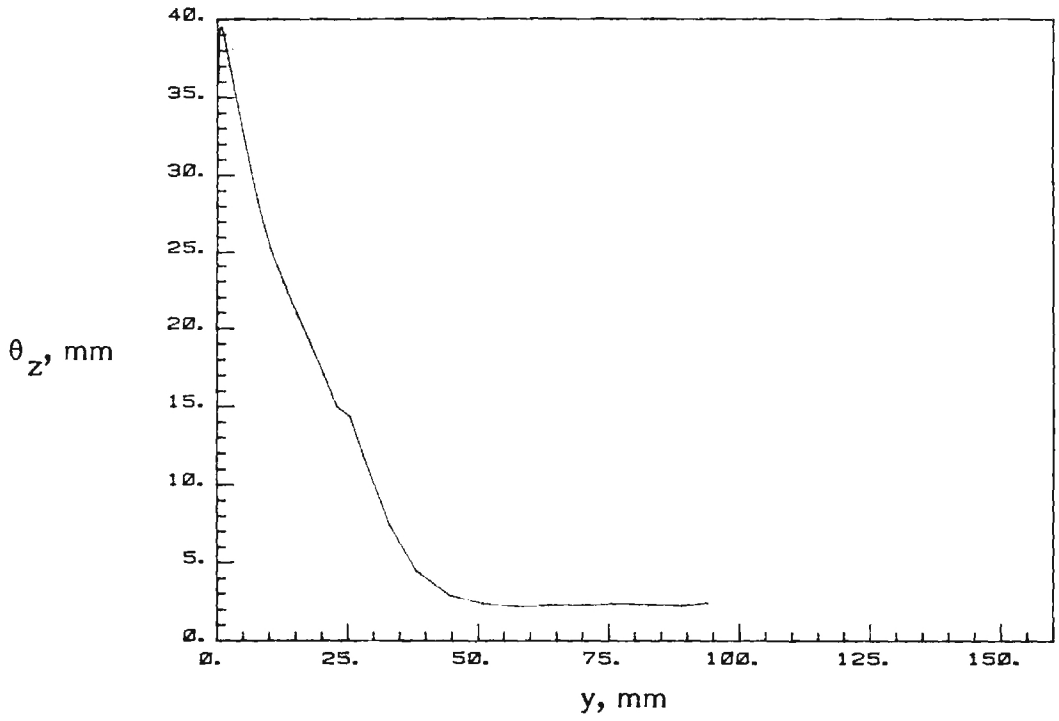

(a) Momentum thickness distribution (z = 152 mm)

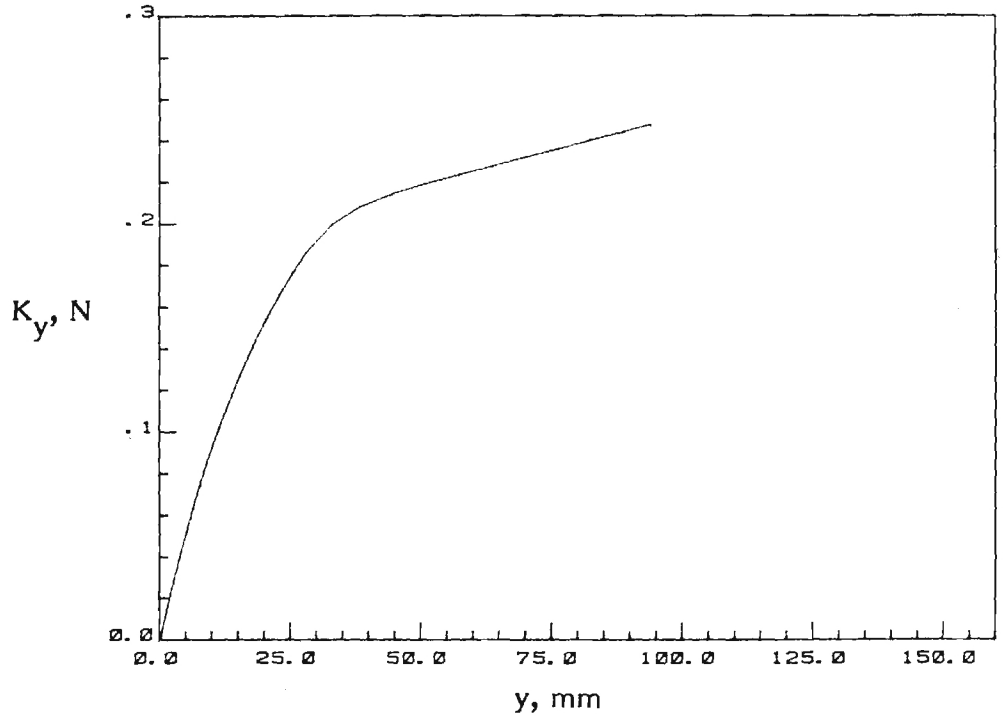

(b) Cumulative momentum deficit.

Figure 20. - Momentum thickness and cumulative momentum deficit along body in juncture.